International Journal of Rock Mechanics & Mining Sciences 159 (2022) 105232

Contents lists available at ScienceDirect

International Journal of Rock Mechanics and Mining Sciences

journal homepage: www.elsevier.com/locate/ijrmms

3D Simulations of gas injection on callovo-oxfordian claystone assuming spatial heterogeneity and anisotropy

I.P. Damians [a,b,*], S. Olivella [a,b], A. Gens [a,b]

[a] Department of Civil and Environmental Engineering (DECA), School of Civil Engineering, Universitat Politècnica de Catalunya·BarcelonaTech (UPC), UPC Campus Nord, Jordi Girona 1-3, Building D2, 08034, Barcelona, Spain
[b] International Centre for Numerical Methods in Engineering (CIMNE), UPC Campus Nord, Gran Capità s/n, Building C1, 08034 Barcelona, Spain

ARTICLE INFO

Keywords:
Hydro-gas-mechanical 3D model
Gas flow
Embedded fracture model
Material heterogeneity
Anisotropy

ABSTRACT

A series of gas injection tests on Callovo-Oxfordian (COx) claystone from the Bure underground research laboratory (URL) in France were carried out at the British Geological Survey (BGS). The tests were performed using a triaxial apparatus specifically designed to capture small volumetric strains induced by the injected gas flow and consequent material dilatancy. The long-duration experiments were monitored throughout. Measurements also included pressure, stresses (axial and radial stresses prescribed for each test stage), rate of gas inflow, gas outflow volume as well as pore-pressures observed at various points of the sample. A coupled hydro-gas-mechanical 3D numerical model has been developed to simulate the tests. Initial permeability is assumed heterogeneous throughout the specimen and embedded fractures are incorporated in the formulation. Gas pressure-induced deformations during the test lead to variations of permeability due to changes in matrix porosity and, especially, fracture aperture as well as fracture orientation due to material anisotropy. A programme of sensitivity analyses involving the variation of different aspects and parameters of the model contributes to a better understanding of the phenomena and highlights its complexity. The model is able to reproduce the observed behaviour of the tests.

1. Introduction

1.1. General

The investigation of gas flow through Callovo-Oxfordian (COx) clay rock materials is an active research area involving the development of new experimental techniques and new numerical approaches. Argillaceous rocks (e.g., COx) and clay based engineered materials (e.g., MX-80 bentonite pellets and blocks) are candidate components for multi-barrier systems for isolation of different types of nuclear waste.

Although there is still an incomplete understanding of the full processes taking place, there are a number of relevant contributions in the literature. Marschall et al.[1] characterized argillaceous rocks regarding gas transport properties, Harrington et al.[2] studied the gas transport properties of claystones including by laboratory and *in situ* tests, Arnedo et al.[3] presented modelling work using heterogeneous fields for the transport properties coupled to deformations that incorporated anisotropy.

Examples of studies on COx clay stone microstructure and fundamental hydromechanical properties and behavior can be found in Menaceur et al.,[4] Armand et al.,[5] Desbois et al.[6] and Zhang and Rothfuchs.[7] Belmokhtar at al.[8] have studied the poroelastic properties of the COx claystone. Zhang et al.[9] analyzed mechanical anisotropy through triaxial, cyclic and creep tests on COx claystone samples with different orientations, and, recently, Shi et al.[10] studied the influence of anisotropy and heterogeneity on strain fields and cracking patterns through X-ray micro-tomographic techniques using uniaxial compression samples.

Mahjoub et al.[11] developed a numerical study of the expansion of the argillite rock during gas injection. Yang et al.[12] performed 3D hydro-mechanical modelling based on the experimental study regarding COx dilatancy through controlled injected gas (helium) flow by Cuss and Harrington[13] and Cuss et al.[14] This paper presents complementary models to better understand the gas flow processes in these experiments.

In the context of bentonitic materials, Harrington et al.[15] studied the development of flow network induced by gas migration in

* Corresponding author. Department of Civil and Environmental Engineering (DECA), School of Civil Engineering, Universitat Politècnica de Catalunya·BarcelonaTech (UPC), UPC Campus Nord, Jordi Girona 1-3, Building D2, 08034, Barcelona, Spain.
E-mail addresses: ivan.puig@upc.edu (I.P. Damians), sebastia.olivella@upc.edu (S. Olivella), antonio.gens@upc.edu (A. Gens).

https://doi.org/10.1016/j.ijrmms.2022.105232
Received 17 January 2022; Received in revised form 21 June 2022; Accepted 28 September 2022
1365-1609/© 2022 The Authors. Published by Elsevier Ltd. This is an open access article under the CC BY-NC-ND license (http://creativecommons.org/licenses/by-nc-nd/4.0/).

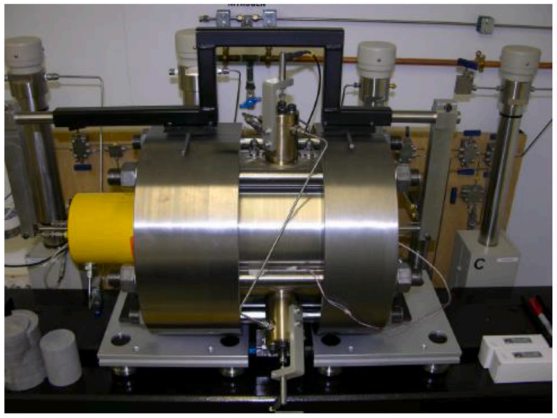

a)

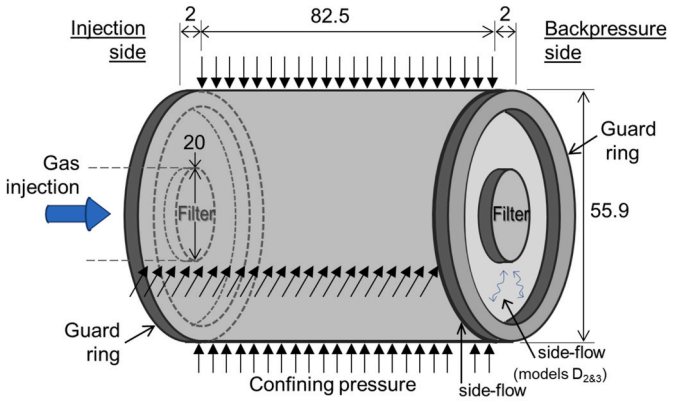

b)

Fig. 1. (a) Experiment set up for the gas flow test on Callovo-Oxfordian claystone (Cuss and Harrington, 2011), and (b) schematic geometry/dimensions (in mm) of the COx specimen, filters and guard-rings.

pre-compacted bentonite. Damians et al.[16] presented sensitivity modelling of gas flow phenomena in MX-80 bentonite where material heterogeneity coupled with an embedded fracture approach played the main role in the simulations. These contributions focus on the fact that gas migration takes place through preferential paths instead of being a uniform process of nonlinear diffusion.

Although the experimental and numerical investigations carried out regarding COx claystone are substantial, at present there is not a common approach to model the coupled behavior during gas migration compared to other kind of problems (for instance, approaches for the coupled THM response of porous media and mechanics with advection/diffusion of heat using effective stress theory are quite similar among researchers and codes). The main reason is that gas migration is a difficult problem involving issues regarding path formation in anisotropic heterogeneous media, high capillary pressures, where modification of local hydraulic properties due to dilatancy are added to the difficulty of characterizing relative permeability and desaturation. Classical approaches for homogeneous porous media that consider a retention curve as a nonlinear function of capillary pressure, and permeability as nonlinear function of saturation (or capillary pressure) are insufficient to provide a satisfactory representation of the processes taking place.[17,18] It seems that material heterogeneity and local deformability play a major role and material properties do not remain constant during the gas flow process. The initial structure of the medium is not homogeneous and changes in structure and hydraulic properties can be caused by deformation. In this paper, the general approach for multiphase flow modelling in deformable porous media is considered together with additional features that have been incorporated with the objective to reproduce the formation of preferential paths for gas migration.

This study contains an application of the approach presented by Olivella and Alonso.[19] In that paper, several aspects of gas flow in clay materials where discussed and a relatively simplified approach was proposed. The fact that this approach is simple is what makes it attractive. Using intrinsic permeability with cubic of aperture, capillary pressure inversely proportional to aperture, and aperture estimated from deformations (including a threshold) makes the model robust as it does not depend on the mechanical constitutive formulation used. So, in principle, it can be combined with any mechanical model and any formulation for the calculation of localized deformations. In this paper, linear elasticity is assumed without loss of generality.

1.2. *Description of the gas injection test*

Gas flow experiments have been carried out at the British Geological Survey (BGS)[20] on a Callovo-Oxfordian (COx) claystone cylindrical sample to investigate the capability of this rock to permit gas migration. Test sample was oriented parallel to bedding, and stress and pore pressure conditions were derived from those of the Bure URL in France, at a depth of about 500 m. The experiment is fully described in[13] and [14].

Fig. 1a displays the experimental set-up. Inside, a cylindrical 82.5 mm-long and 55.9 mm-diameter COx sample of 0.466 kg (dry weight) and 14.8% porosity was tested with gas (helium) injection from one of the sample ends. The injection location was centered through a filter (with a smaller area than the total diameter or axial cross-section of the sample at the injection location; see Fig. 1b) whereas a guard-ring device was installed at the circumferential edge of the remaining area with the aim of to preventing side-wall flow as a possible transport mechanism.[14] Both filter and guard-rings were connected to different pore pressure sensors. A similar arrangement was provided at the backpressure end with separate pore pressure sensors in the filter and guard ring. Therefore, four independent pressure measurements were made during test injection. Inflow and outflow flow rates were measured as well as displacements and volumetric deformations with strain gauges glued to the sample. The injection gas pressure was managed through an interface vessel including pipework and the filter, which it is known that play a role in gas pressure and gas flow trend responses both in terms of the resulting shape and achieved magnitudes during test development.[16] Mechanically, the sample had no restriction on the development of volumetric strains because radial displacements were permitted (a rubber sleeve covered the specimen radially, with surrounding triaxial confining fluid cell allowing control of the confining pressure) as well as axial displacements (at backpressure side).

The experimental test carried out lasted more than one year and composed four stages: initial swelling stage (about 22 days duration), equilibration at *in situ* conditions (about 26 days), hydraulic testing (about 80 days), and finally, gas injection testing (more than 270 days duration) with different boundary conditions (see below). The COx sample was kept under a high confinement throughout, specifically, the specimen was subjected to a constant radial and axial stress of 12.5 MPa and 13 MPa, respectively, derived from those of the Bure URL in France at 500 m-depth. The initial pore pressure was 4.5 MPa. The gas was injected into the sample through an interface vessel in a stepwise manner; alternating from a constant gas flow rate, causing a progressive increase of gas pressure, to a condition of constant injection pressure. More details of the experimental test history and stage descriptions/durations can be found in Cuss and Harrington.[13]

Fig. 2 displays the measurements from the gas injection (flow rate in logarithmic scale) stages that ranges from about day 130 to day 400. The results from the test show that the injection pressure was almost constant (from about day 160 and until the end of the text), even after a reduction of the injection flow rate (day 255), gas breakthrough occurred (outflow response achieved at about day 260) and an increase of the resulting pore-pressure at the guard-ring zone was generated

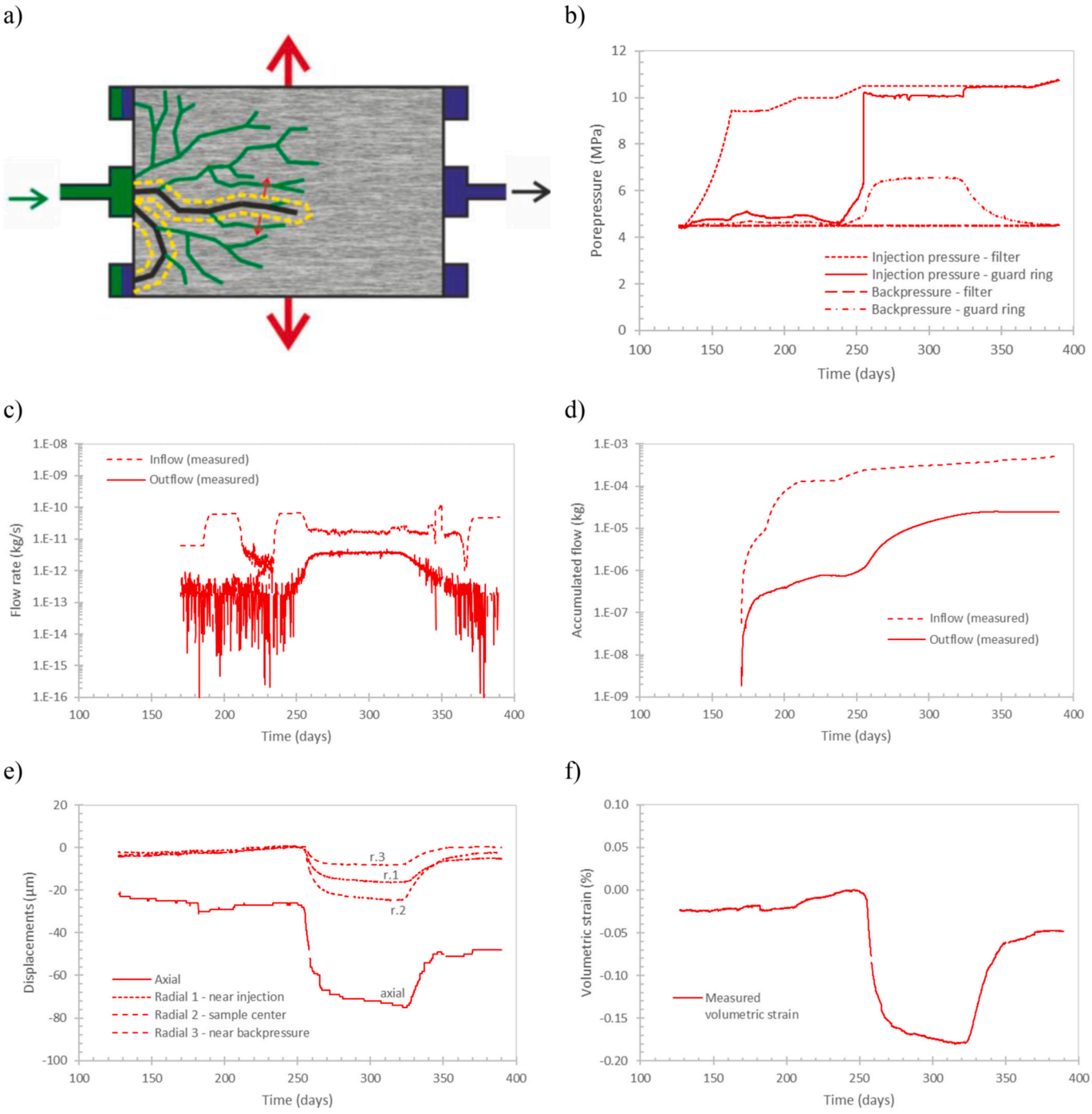

Fig. 2. (a) Schematic representation of tested sample and dilation effect of (b) pore-pressures, (c) flow rates, (d) accumulated mass (integrated from 165 days), (e) displacements and (f) volumetric deformations for the experiment on the COx sample. (Modified from [11]).

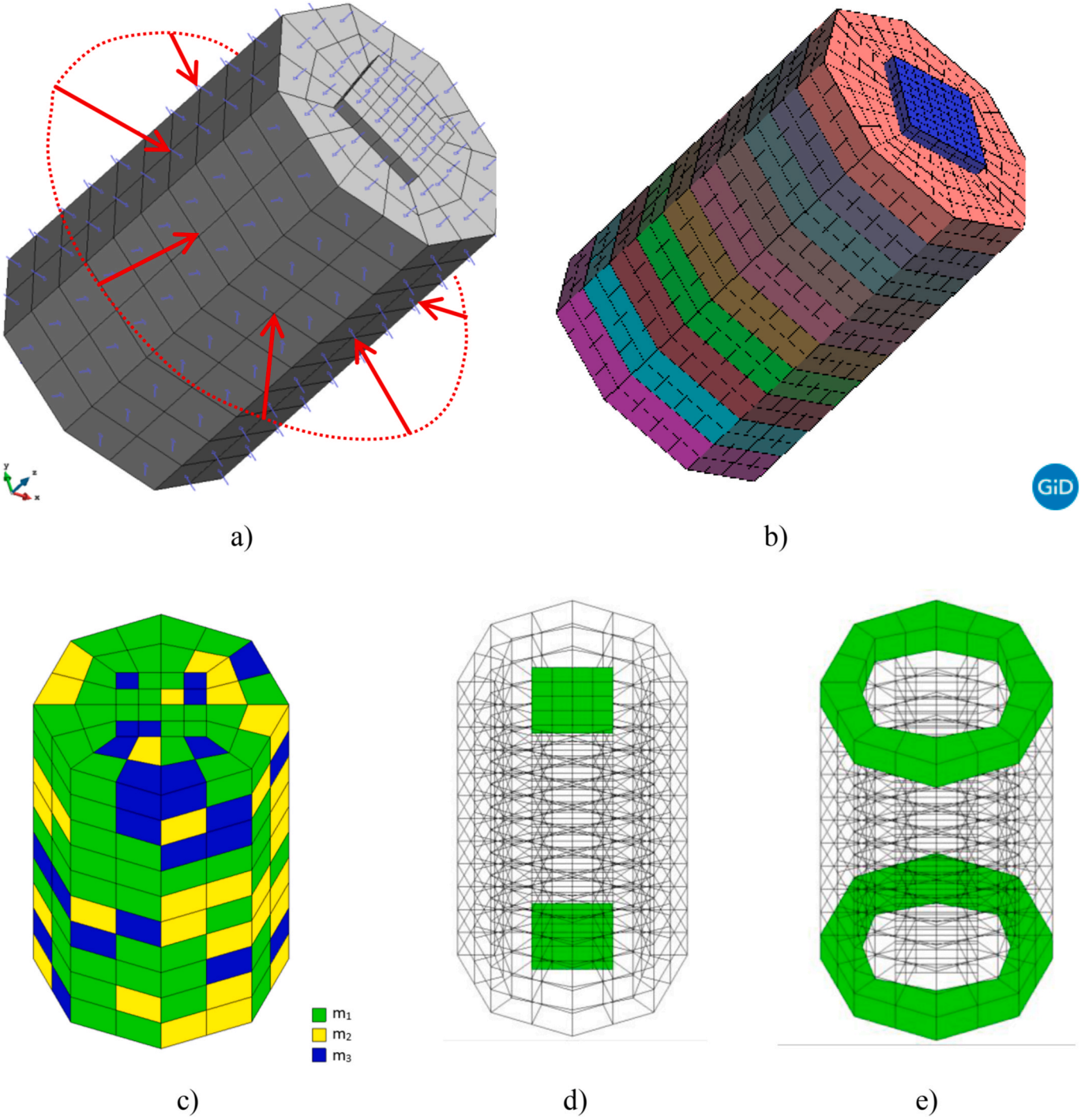

Fig. 3. (a) Geometry of the model (sample and filters); the arrows (red and small blue) indicate the applied stresses, (b) detail of the layered finite element mesh used for the calculations, (c) model geometry incorporating material heterogeneity, (d) detail of the filters, and (e) additional volumes that permit to model the effect of the guard-rings volume. (For interpretation of the references to color in this figure legend, the reader is referred to the Web version of this article.)

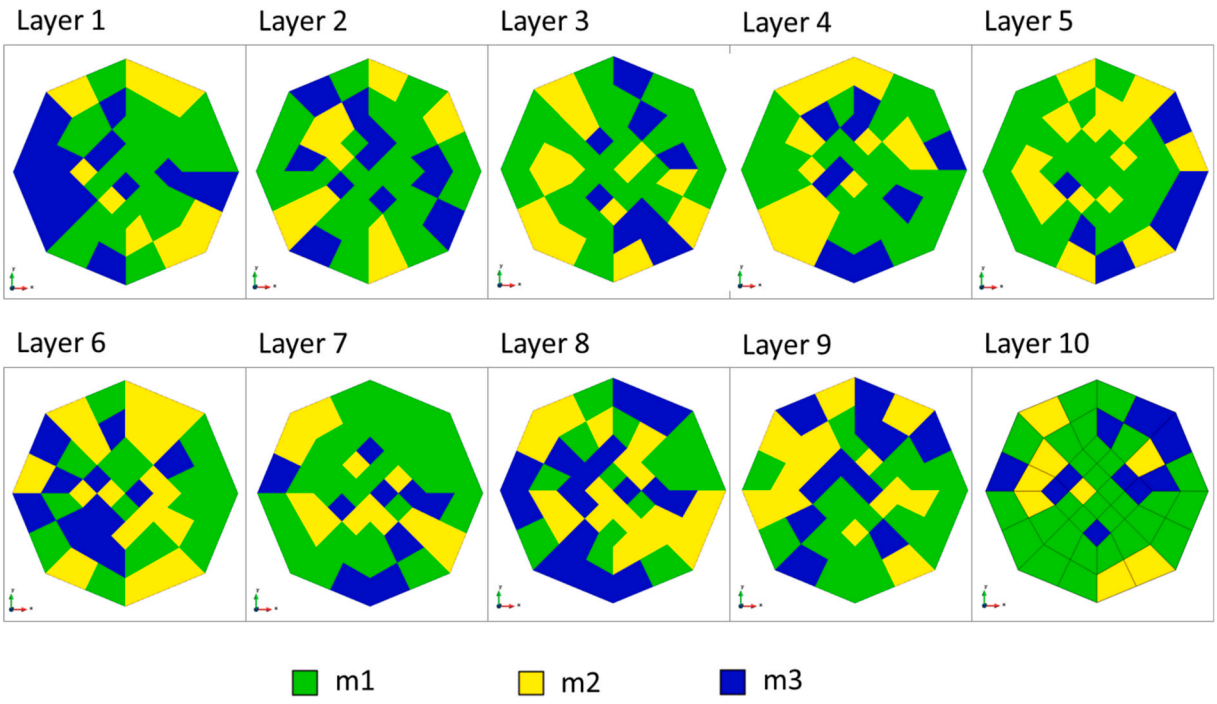

Fig. 4. Distributions of materials m1, m2 and m3 in the different layers of the sample (see Table 1).

reaching a similar pore-pressure magnitude as at the injection filter. Advective flow into the sample is identified to begin through the gas pressure response at guard-rings, which may be inferred to occur at about day 240 (compare Fig. 2b and c). Therefore, up to day 240, only diffusive gas movement was occurring. Regarding the mechanical performance, the breakthrough generated both radial and axial dilation of the sample, in addition to an increase of the outflow rate. After about 70–80 days from the breakthrough (i.e. after about 320 days from the beginning of the test), dilation and outflow stopped; essentially a shut-off event. At this point, both radial and axial displacements (i.e., volumetric strains), as well as the outflow rate and guard-ring back-pressure, exhibited a sudden trend reversal and almost recovered to the same magnitudes as observed prior to the breakthrough.

In this study, a 3D Hydro-Gas-Mechanical (HGM) Finite Element (FE) model has been developed and all the available measurements have been compared with the obtained numerical results. The computer code CODE_BRIGHT[21,22] has been used in the analyses. The numerical formulation was able to simulate the performance up to the breakthrough event and subsequent dilation phase. However, the halt in gas outflow and consequent mechanical shrinkage are difficult to explain and are not captured by the numerical model proposed at this stage (without changing the boundary conditions). Accordingly, the main scope of this study at this point is to consider the test data up to 320 days to describe the gas pressure generation and the dilation behavior (i.e. up to the flow shut-off point and contraction of the sample).

2. Modelling approach

2.1. Model geometry and initial/boundary conditions

An octagonal prism (rather than a cylindrical prism) was considered to model the test on the COx sample (Fig. 3). This geometry facilitates the application of the radial boundary condition due to the flat surfaces (Fig. 3a). The modelled sample is divided into 10 layers. Each layer is composed of 48 sub-volumes with sizes between 80 mm^3 (inner part) and 670 mm^3 (outer part) (see Figs. 3b and 4 with layer-by-layer sample detail). Additional 2 × 16 vol were generated to include the representation of the injection and back-pressure filters (the square centered volumes shown in Fig. 3b and e represents the back-pressure filter). Although square shaped, the modelled filter geometry is consistent with the actual circular filter surface and actual volume used in the test (i.e., about 0.3 ml including the volume of additional devices such as pipes). This different geometry was due to mesh compatibility and it was not expected to cause any significant effects on the results from the analyses.

The sub-volumes indicated in Fig. 3c have been used to incorporate an initial random heterogeneity through the definition of three different materials (m1, m2, and m3; see Fig. 4) with different properties according to expected initial intrinsic permeability variability (see[16] for methodology details and sensitivity for the followed material heterogeneity strategy). Inclusion of heterogeneity is important because advective flow of gas in low-permeability materials appear to occur through preferential flow paths along the weakest parts of the specimen[15,16]. An initial heterogeneity incorporated into a continuum approach provides a way to capture this behaviour more realistically. The final mesh used comprises 5097 nodes in 4352 hexahedral elements.

The initial conditions considered in the analysis are:

- **Hydraulic conditions**: water and gas pressures were prescribed to $P_l = 4.5$ MPa and $P_g = 0.1$ MPa, respectively. Water saturation was assumed to be 1. The initial material porosities were prescribed to be 0.145, 0.150, and 0.155 for the three different materials defined (i.e., m_1, m_2, and m_3; see Fig. 4).
- **Mechanical conditions**: the initial stress tensor was set to $\sigma_x = \sigma_y = -11.5$ MPa (radial compression), and $\sigma_z = -12.5$ MPa (axial compression). After sample saturation and until the end of the test, stresses were assumed to be $\sigma_x = \sigma_y = -12.5$ MPa (confining

Table 1
Model material properties assumed for COx sample.

Constitutive equation	Parameter name	Symbol		Value
Elasticity	Young's moduli [(b)]	$E_1 = E_2$ (MPa)		8500
	Anisotropy ratio (E_1 /E_3)	α (−)		2.43
	Poisson Ratio	ν (−)		0.3
Retention curve	Pressure parameter	p_0 (MPa)		22.68
	Shape parameter	λ (−)		0.396
	Minimum Saturation	S_{min} (−)		0
	Maximum Saturation	S_{max} (−)		1
Intrinsic permeability [(a)] (k_{ii})	Matrix Permeability, parallel	$k_{11} = k_{22}$ (m^2)	m_1	3.2×10^{-20}
			m_2	3.6×10^{-20}
			m_3	4.0×10^{-20}
	Matrix Permeability, perpendicular	k_{33} (m^2)	m_1	4.0×10^{-21}
			m_2	5.0×10^{-21}
			m_3	6.0×10^{-21}
	Reference porosity	φ_0 (−)	m_1	0.148
			m_2	0.163
			m_3	0.187
	Initial aperture	b_0 (m)	m_1	1.5×10^{-9}
			m_2	5.0×10^{-9}
			m_3	9.5×10^{-9}
	Spacing	a (m)	m_1	5.0×10^{-6}
			m_2	5.0×10^{-5}
			m_3	5.0×10^{-4}
	Threshold strain	ε_0 (−)	m_1	5.0×10^{-4}
			m_2	3.0×10^{-4}
			m_3	1.0×10^{-4}
	Maximum aperture	b_{max} (m)	m_1	1.5×10^{-7}
			m_2	3.5×10^{-7}
			m_3	7.5×10^{-7}
Liquid relative permeability	Power of saturation degree	n_l (−)		3
Gas relative permeability	Power of saturation degree	n_g (−)		2
	Maximum gas saturation	S_{gmax} (−)		0.3
Dissolved gas diffusion	Tortuosity parameter [(c)]	τ (−)		(see Table 2)

Notes.
[a] For intrinsic permeability, three different parameter values are distributed within the modelled sample to incorporate an initial random material heterogeneity between m_1, m_2, m_3 material zones definition (see Fig. 4).
[b] Young's modulus considered for reference case is an upper bound of what is considered for COx; sensitivity cases using lower values are also presented.
[c] Different values of tortuosity (defined as straight path length divided by real path length) were assumed in order to analyze the effect dissolved gas diffusion; this model sensitivity was required to fit the gas pressure response at guard-rings.

pressure) and $\sigma_z = -13.0$ MPa (axial stress), according to test specifications and in line with *in situ* stresses representative of the Bure URL.

The prescribed boundary conditions are:

- **Hydraulic conditions**: water and gas pressures were prescribed at the injection filter, according to the values given in[13]. Water pressure was prescribed to be 4.5 MPa during the first saturation and equilibration stages, increased up to 8.5 MPa, returned to 4.5 MPa before 127 days. The gas injection pressure was increased from $P_g = 0.1$ MPa (atmospheric assumption) up to 4.5 MPa before 127 days. Afterwards, gas pressure varied according to the test stages specified and liquid pressure was no longer prescribed.
- **Mechanical conditions**: displacements were prescribed to be zero in the axial direction at the injection surface. Displacements were not prescribed on the lateral surface and on the back-pressure surfaces (where confining and axial stresses are applied, respectively).

Some preliminary calculations considering the sample and filters only (see previous Fig. 3b; with no guard-rings defined yet) demonstrated that the observed pressure in the guard-ring zone was, at first, difficult to reproduce. As indicated above, the measurement of pressure at the guard-rings showed an important delay compared to the prescribed pressure in the injection zone (i.e., through the modelled filter volume only). For this reason, it was decided to include and to calibrate the volumes to represent the guard-rings (Fig. 3e). A volume correction factor VF (defined as fluid-available volume divided by total volume) was used in the additional guard-rings domain to adjust the volume for the injection and back-pressure guard-ring devices, to a realistic value. This is so due to the resulting data reception may be influenced by the existent volume between the sample (i.e., the actual occurrence of the response development) and the sensor (i.e., the received/appearance response development).

2.2. Constitutive model and governing equations

The hydro-gas-mechanical (HGM) model is a heterogeneous continuous two-phase domain, where the standard equations of balance of water, balance of gas and equilibrium of stresses are solved. The material properties used in the analysis correspond to the following constitutive models:

- Anisotropic elasticity to represent the mechanical behavior.
- Anisotropic intrinsic permeability including embedded discontinuities with permeability calculated using the cubic law. Intrinsic permeability therefore changes with element deformations in accordance with the embedded discontinuity aperture, as described below.
- Retention curve (Van Genuchten) to relate fluid saturation to capillary pressure.
- Relative permeability defined as the fluid saturation raised to a power.
- Diffusion of the dissolved gas, represented by Fick's law incorporating a tortuosity coefficient. The computer code used (CODE_BRIGHT[22]) takes a value of 4.0×10^{-9} m^2/s for the diffusivity of dissolved gas by default.
- The basic gas diffusion coefficient is multiplied by the tortuosity coefficient, porosity and the gas degree of saturation to obtain the effective diffusion coefficient.

It is assumed that any point in the medium may undergo intrinsic permeability variations induced by deformation. Heterogeneity provides a non-uniform field which is intended for initiation of preferential path formation. Gas propagates first by molecular diffusion and dispersion. These fluxes develop a gradient of concentration. As concentration of dissolved gas increases, the corresponding gas pressure (Henry's law) may lead to desaturation at certain zones (not uniformly because gradients are not uniform due to heterogeneity). As gas begins to propagate by advection in the elements that have enhanced permeability, connection between them is progressively developed. The approach is based on a network that develops induced by the flow. Obviously, this network depends on the initial heterogeneity distribution, but the effect of that distribution is beyond of the scope of this study.

Implicit embedded fractures are incorporated into the standard formulation to allow the representation of preferential paths. The global intrinsic permeability is defined as a function of both material matrix and internal fracture permeabilities, as:

$$k_{\text{intrinsic}} = k_{\text{matrix}} + k_{\text{fractures}} \tag{1}$$

whereas liquid- and gas-phase permeabilities are described by

$$k_{\text{liquid}} = \left(S_{\text{eff,liquid}}\right)^{n_{\text{liquid}}} \left(k_{\text{matrix}} + k_{\text{fractures}}\right) \tag{2}$$

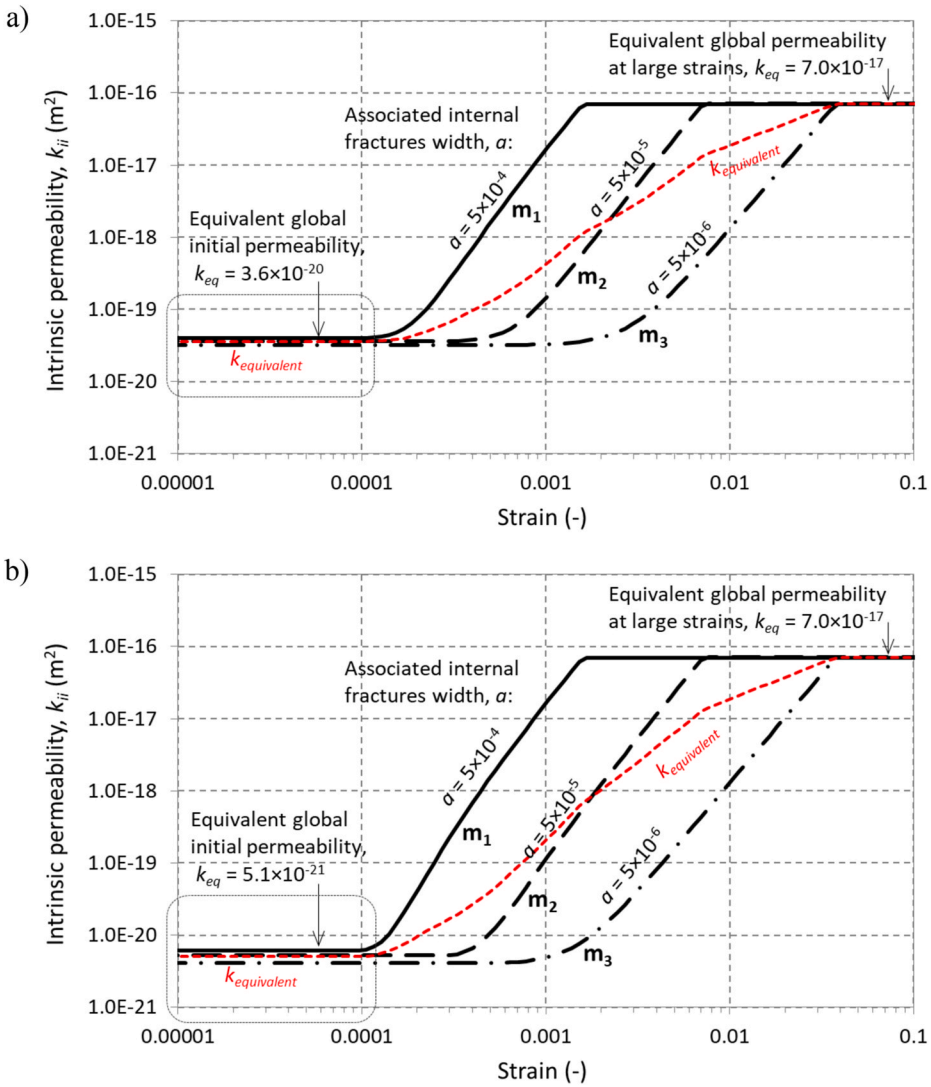

Fig. 5. Intrinsic permeability evolution due to strain development: (a) parallel (i.e., $\beta = 90°$): and (b) perpendicular (i.e., $\beta = 0°$) to bedding.

Table 2
Volume factor of the guard-rings and tortuosity of dissolved gas sensitivity cases.

Model cases:	Guard-ring volume factor[(a)], VF (−)	Tortuosity, τ (−)	Anisotropy: Bedding layers orientation (β-angle)
Model A	0.50	0.05	Axial (β = 90°; bedding parallel to axial direction)
Model B	0.20	0.05	Axial (β = 90°)
Model C	0.0 (no guard-ring)	0.05	Axial (β = 90°)
Model D_0 [(b)]	0.20	0.10	Axial (β = 90°)
Model E	0.50	0.05	Tilted (β = 60°)
Model F	0.50	0.05	Tilted (β = 30°)
Model G	0.50	0.05	Radial (β = 0°; bedding orthogonal to axial direction)

Notes.

[a] According to the modelled volume representing the actual injection guard-ring, VF values of 0.5 correspond to about 5 ml, whereas VF = 0.2 corresponds to 2 ml. Both values are of the same order of magnitude as the actual ones as per indication of the test authors.

[b] Model D is later presented as the best fitting model and, consequently, three complementary cases on D_0 were generated: D_1, where the backpressure side has a permeability of 1×10^{-18} m² (i.e., allowing backpressure side-flow to occur and hydraulic connectivity between filter and guard-ring); D_2, with a 33% stiffness reduction (i.e., $E_{D2} = (1/3)E_{D0} = 2833$ MPa, see text for details); and D_3, with both side-flow and stiffness reduction conditions.

$$k_{gas} = \left(S_{eff,gas}\right)^{n_{gas}^{matrix}} k_{matrix} + \left(S_{eff,gas}\right)^{n_{gas}^{fractures}} k_{fractures} \quad (3)$$

respectively, with $S_{eff,liquid/gas}$ (−) representing the effective degree of saturation for liquids or gases and $n_{liquid/gas}^{matrix/fractures}$ a power parameter for each case (i.e., for liquid or gas state, and for matrix or fractures media; see Table 1). Porous media tend to have relative permeability proportional to degree of saturation to a power in the range of 3–6 (obtaining curves similar to Van Genuchten relative permeability) while fractures tend to have power between 1 and 2.[17]

The matrix permeability component is calculated as (Kozeny-Carman's type equation[23]):

$$k_{matrix} = \frac{k_0(1-\varphi_0)^2}{\varphi_0^3}\frac{\varphi^3}{(1-\varphi)^2} \quad (4)$$

where k_0 (m²) is the initial permeability (randomly distributed along the material), φ_0 (=0.44) is a reference porosity and φ (−) is the current porosity value that varies in space and time during the test.

The embedded fracture permeability is defined by the cubic law as follows, which is useful for coupled modelling in rocky media[24]:

$$k_{fractures} = \frac{b^3}{12a} \quad (5)$$

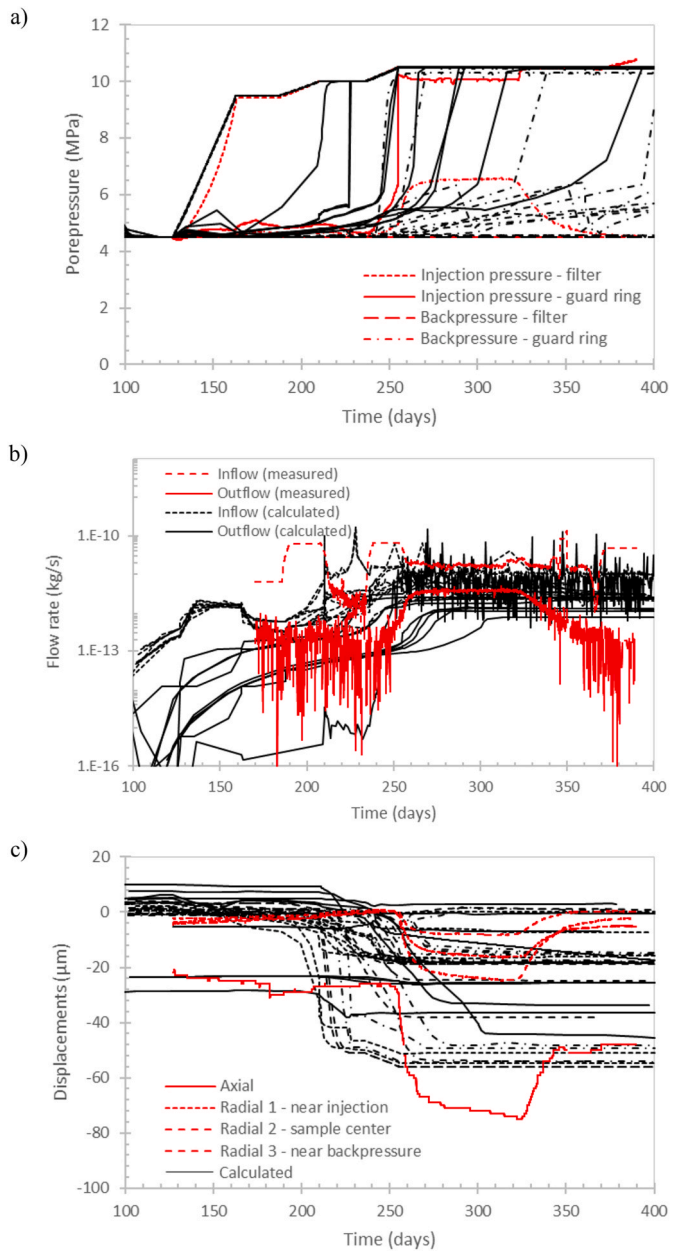

Fig. 6. Summary of results from all sensitivity cases modelled (black curves) compared with measured data (red curve) for the experiment on the COx sample on (a) pore-pressures, (b) flow rates, and (c) displacements. (For interpretation of the references to color in this figure legend, the reader is referred to the Web version of this article.)

where a denotes the associated internal width for each fracture (equivalent to the assumed spacing between fractures) and b (m) is the aperture of the fractures. The value of b depends on the volumetric strain ε (−) as

$$b = b_0 + \langle \varepsilon - \varepsilon_0 \rangle a \leq b_{\max} \tag{6}$$

with b_0 (m) and $b_{\max}$ (m) being the initial and maximum aperture of the fractures and ε_0 a threshold strain (see Table 1). Modelling with variable strain-dependent intrinsic permeability can be crucial for THM modelling in fractured rocks.[25]

In equations (2) and (3), liquid and gas relative permeabilities are defined by the effective saturation degree of liquid and gas respectively. Hence,

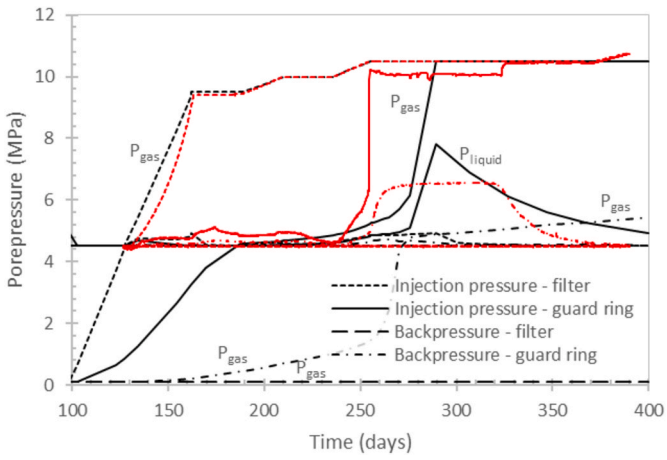

Fig. 7. Evolution of injection pressure and back-pressure (Model A).

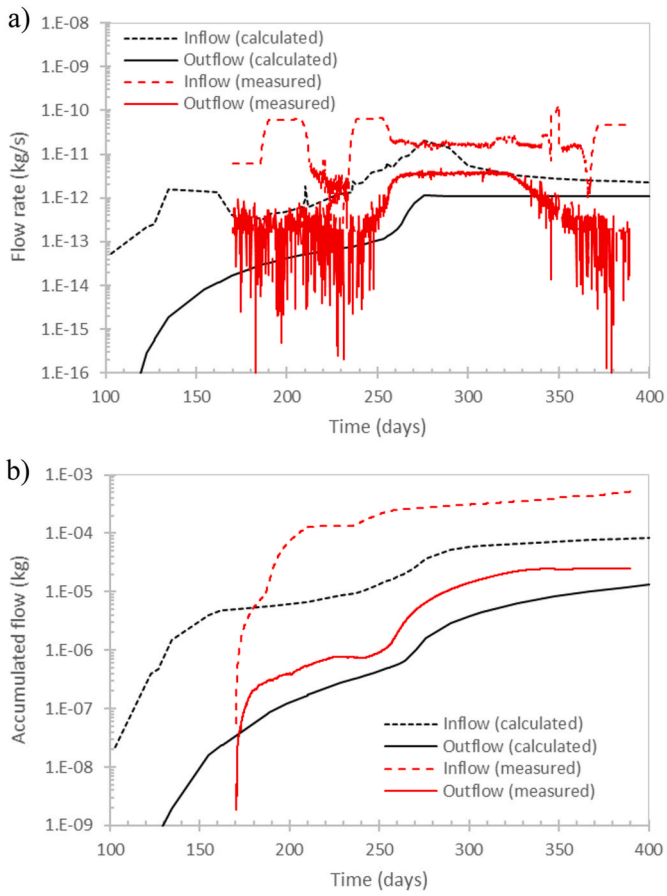

Fig. 8. (a) Flow rate and (b) accumulated flow of gas for inflow and outflow ends (Model A).

$$k_{r,\text{liquid/gas}} = \left(S_{\text{eff,liquid/gas}}\right)^{n_{\text{liquid/gas}}} = \left(\frac{S_{\text{liquid/gas}} - S^{\min}_{\text{liquid/gas}}}{S^{\max}_{\text{liquid/gas}} - S^{\min}_{\text{liquid/gas}}}\right)^{n_{\text{liquid/gas}}} \tag{7}$$

The retention curve may change with the opening of fractures as pore size controls gas entry values, and fractures may play the role of large pores, leading to a reduction of gas entry pressure. The capillary pressure can then be calculated as

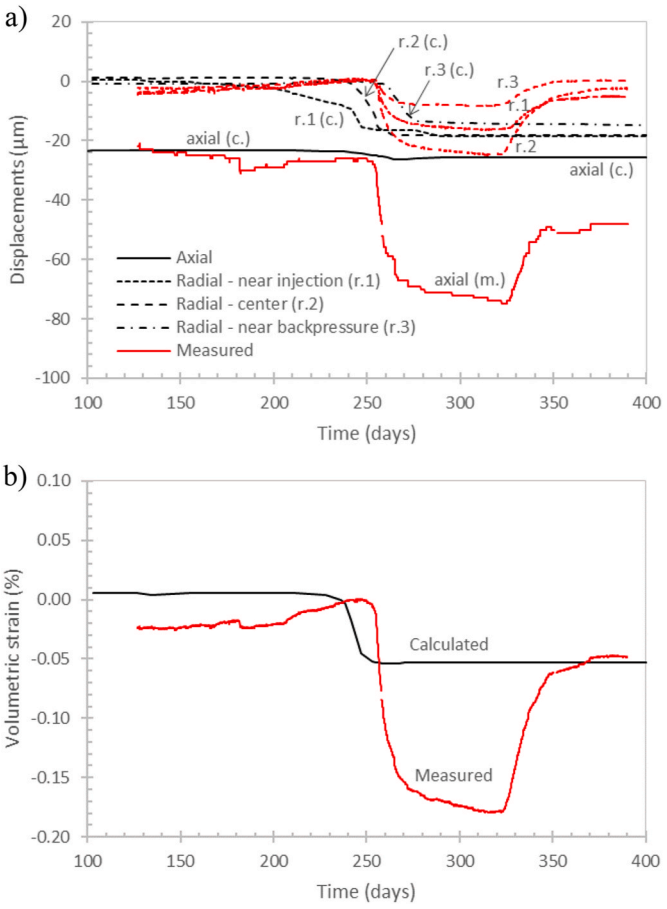

Fig. 9. (a) Evolution of displacements and (b) volumetric deformation (Model A).

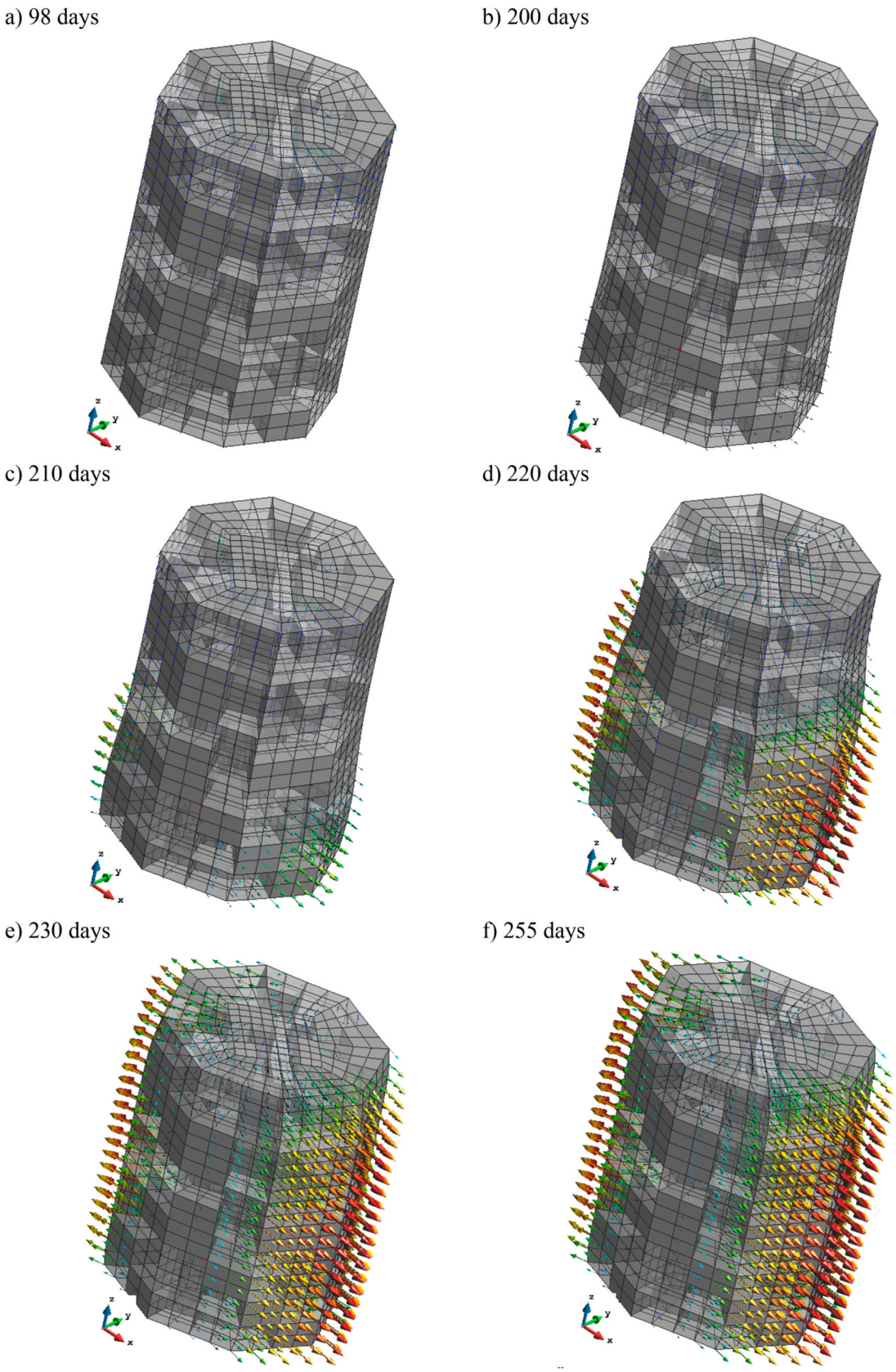

Fig. 10. Displacement vectors and deformed mesh obtained during test development at (a) 98, (b) 200, (c) 210, (d) 220, (e) 230, and (f) 255 days. (Model A).

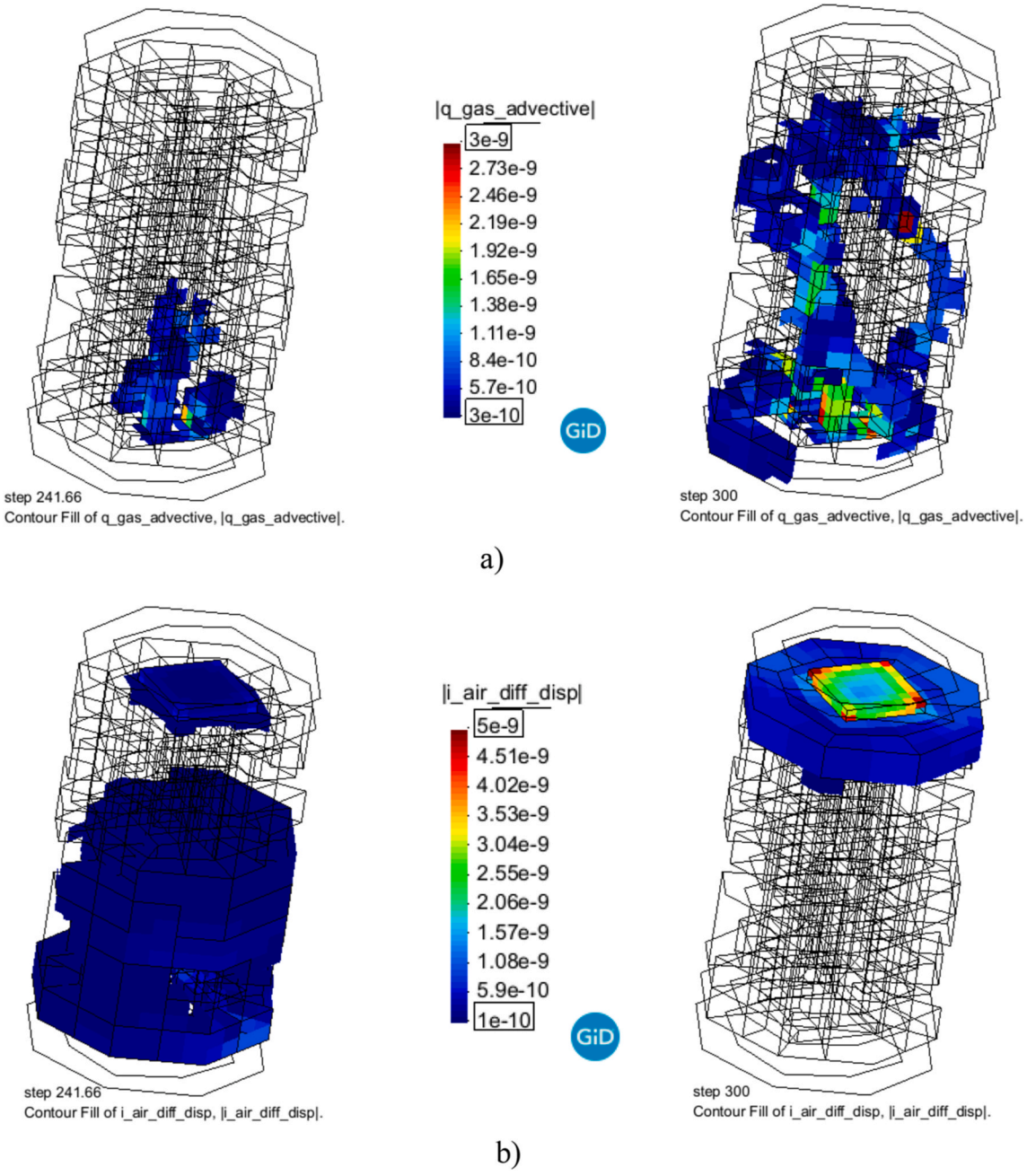

Fig. 11. Magnitude of (a) gas advective flux (m/s) and (b) dissolved gas diffusive flux (kg/m^2/s) before (left) and after (right) breakthrough (injection at the bottom of the sample). (Model A).

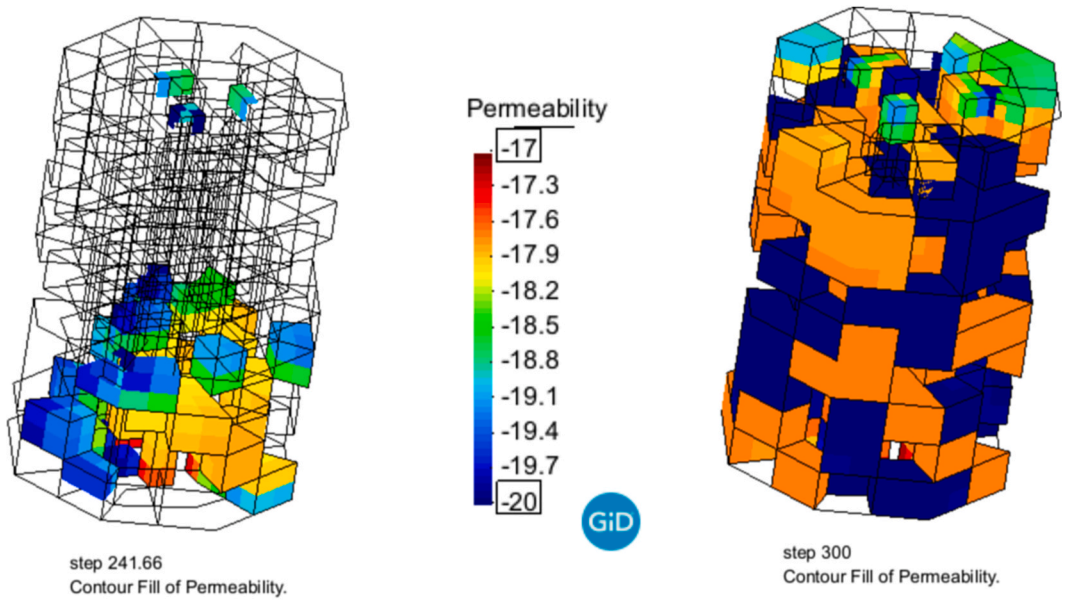

a)

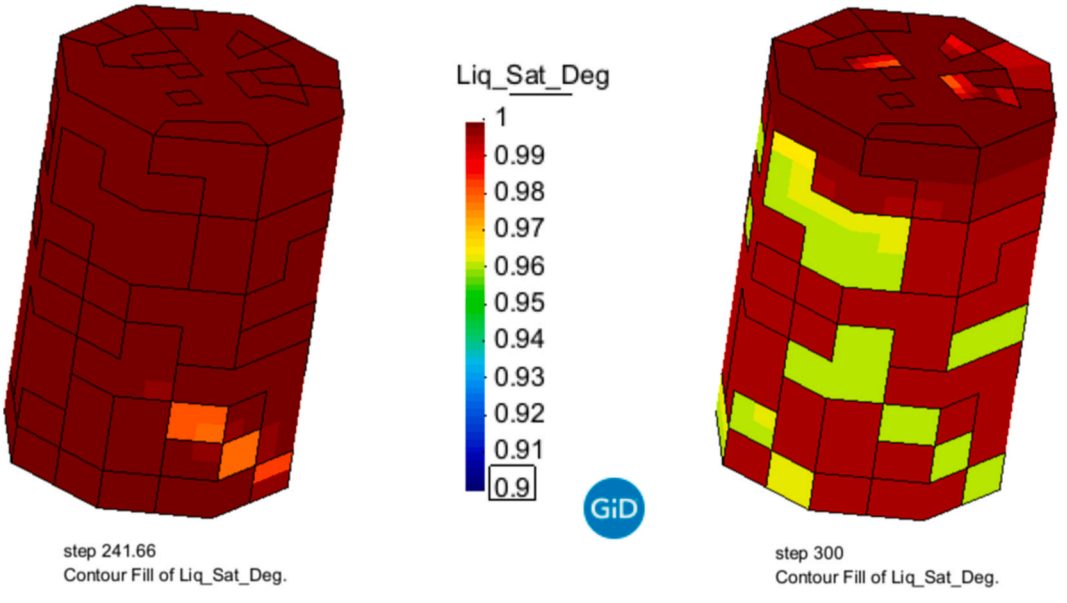

b)

Fig. 12. (a) Permeability and (b) degree of saturation before (left) and after (right) breakthrough. (Model A). (Note: no color in a-figure means results below the plotted range specified, i.e., permeability $<1 \times 10^{-20}$). (For interpretation of the references to color in this figure legend, the reader is referred to the Web version of this article.)

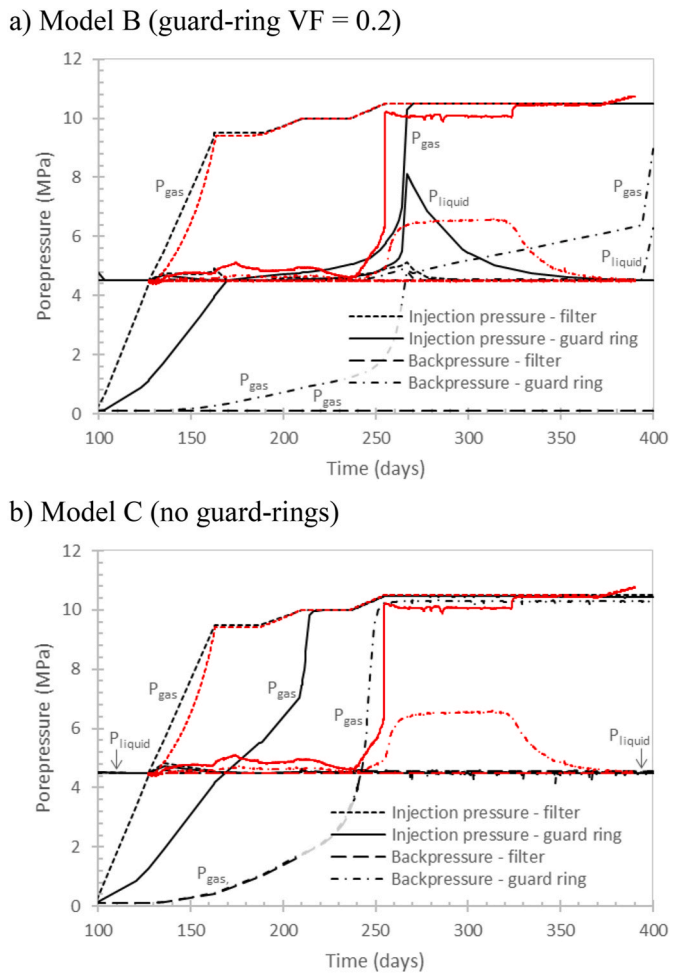

Fig. 13. Comparison of pressures for Models B and C.

$$p = p_0 \sqrt[3]{\frac{k_0}{k}} \tag{8}$$

where p_0 and k_0 are capillary pressure and intrinsic permeability corresponding to the initial conditions at certain point while p and k correspond to the deformed state at that point.

As specified, more details on this formulation can be found in CODE_BRIGHT user's guide.[22]

3. Material properties

3.1. General

Table 1 contains the material properties that have been used to carry out the coupled modelling of water and gas injection in the COx specimen. When not explicitly detailed in the sourcing test document[12,13], different other references were considered in order to assume realistic/feasible material parametrization[2–9] and/or analogous modelling strategies[15,16].

Fig. 5 shows the parallel (i.e., k_{11} and k_{22} main directions) and perpendicular (i.e., k_{33} direction) bedding intrinsic permeability (k_{ii}) response to strain changes for the assumed m_1, m_2, and m_3 materials, as well as the resulting global-equivalent permeability of the whole sample.

3.2. Model sensitivity

Several model case results are presented in this section, as listed in

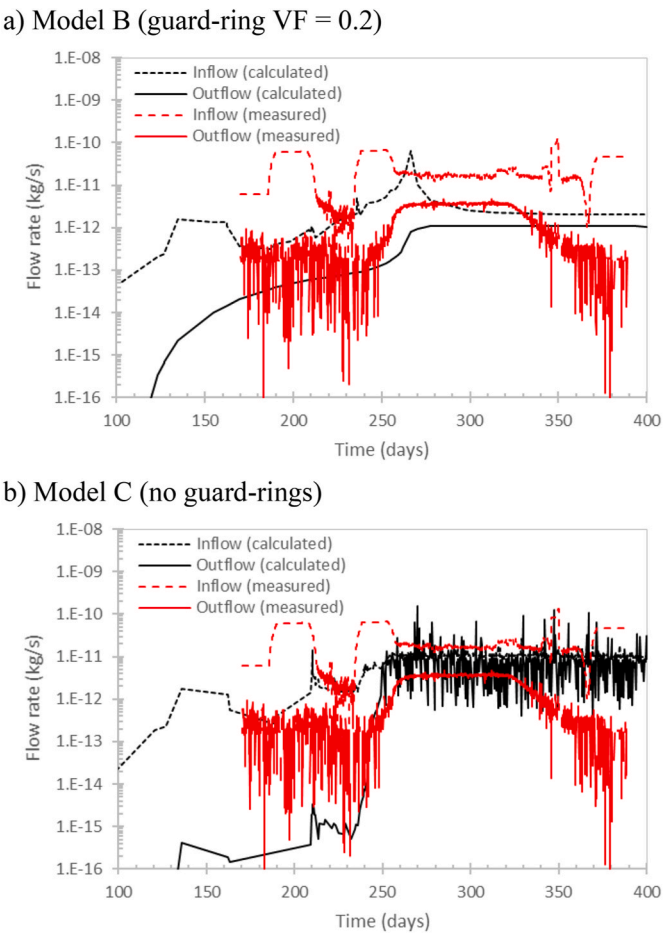

Fig. 14. Comparison of gas inflow and outflow rates for Models B and C.

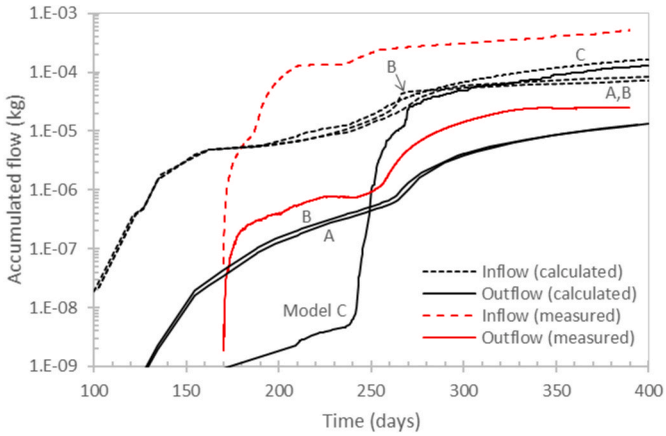

Fig. 15. Comparison of accumulated gas inflow and outflow for Models A, B, C (experimental values have been integrated from 165 days).

Table 2. Modelling this experiment was a challenging task and several uncertainties had to be resolved. The differences among the cases presented for the sensitivity analyses involve mainly variations of guard-ring volume, dissolved-gas tortuosity, and sample's embedded fracture orientation. An initial model (Model A) is described first together with representative results. This first model was not calibrated against the experimental data. The other sensitivity cases considered are called Model B, C, D (D_0), F and G, in which guard-ring volume factor (VF), dissolved air tortuosity, and embedded fracture orientation were

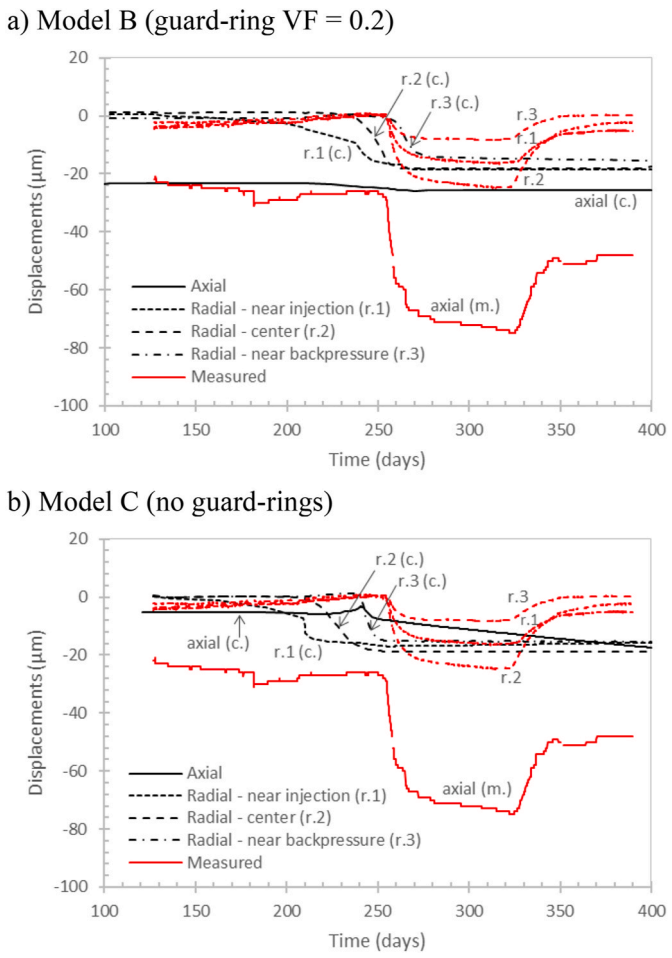

Fig. 16. Comparison of radial and axial displacements for Models B and C.

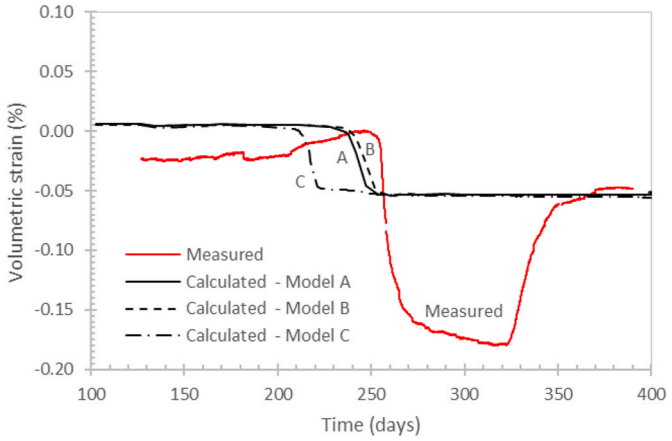

Fig. 17. Comparison of sample volumetric deformation for Models A, B, C. Sensitivity on guard-ring volume factors.

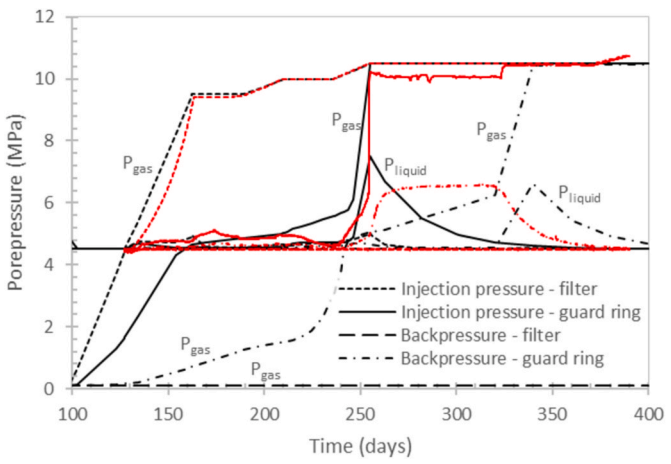

Fig. 18. Evolution of injection pressure and back-pressure for Model D_0 ($\tau = 0.1$).

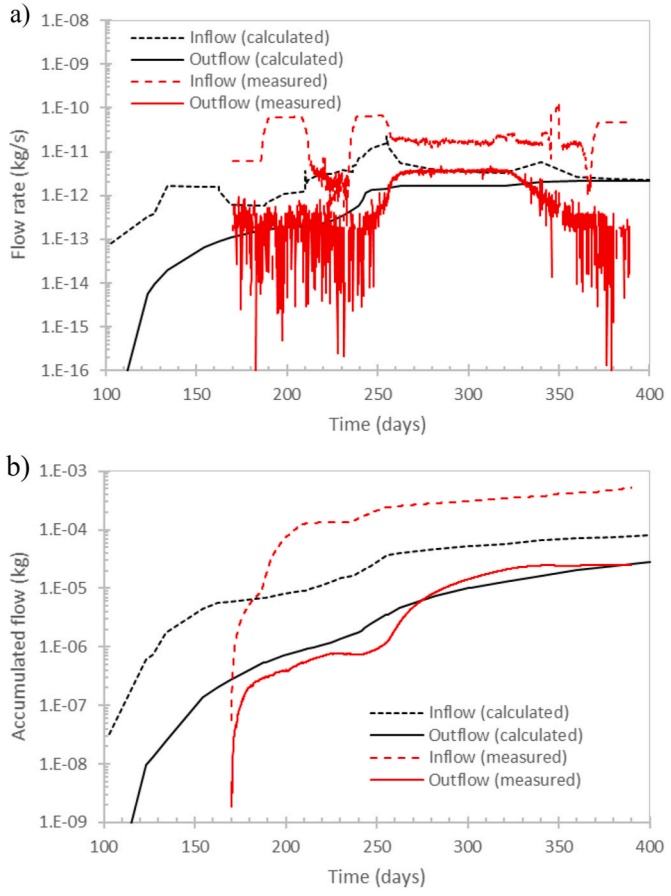

Fig. 19. (a) Flow rate and (b) accumulated flow of gas for inflow and outflow (Model D_0; $\tau = 0.1$).

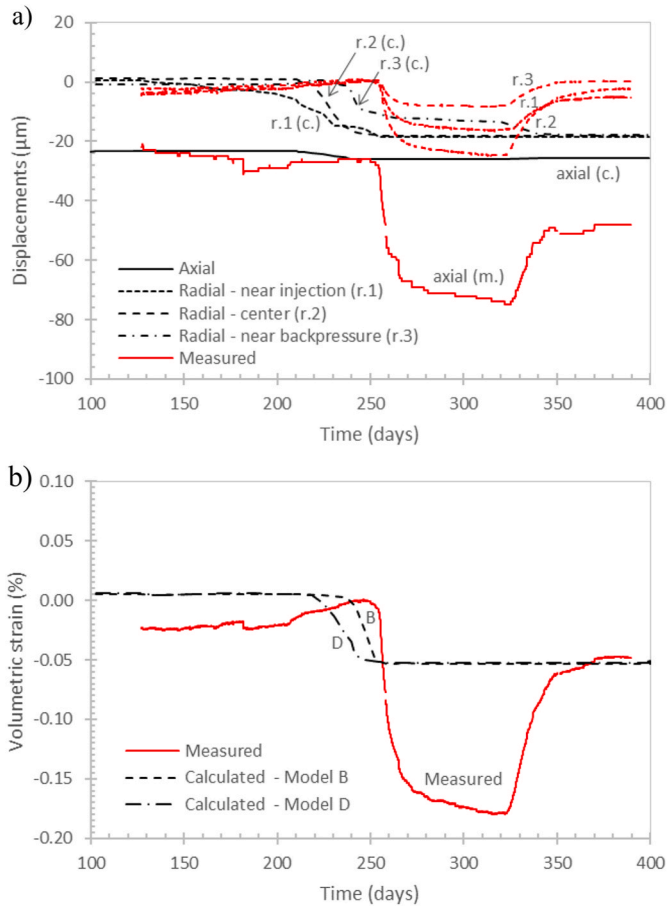

Fig. 20. (a) Radial and axial displacements for Model D_0 ($\tau = 0.1$) and (b) comparison of sample volumetric deformation for Models B and D_0. Sensitivity on dissolved gas diffusion tortuosity.

modified one-at-the-time from Model A assumptions. Although the test equipment volumes (pipes, vessels, filters, etc.) can be estimated, accurate values may be difficult to determine. Thus, a suitable modelling strategy may include their calibration, in this case, through volume factor to the guard-rings (which, as specified, are connected to different pressure sensors).

Three additional models were generated based on Model D_0 (where VF and tortuosity were changed from Model A; see Table 2) for a lower material stiffness assumption (Model D_1), backpressure side-flow with higher permeability or sample's side connectivity (Model D_2), and both stiffness reduction and backpressure side-flow variations (Model D_3). This higher permeability effect at the surface contact with the sample and both the guard-ring and the filter (see Fig. 1b "side-flow" detailed zone) was assumed in order to allow faster gas side-flow or, in other words, to generate a hydraulic connectivity between backpressure filter and guard-ring once gas injection achieves that location.

In order to show first the range of response from all model cases, Fig. 6 presents the pore-pressure, flow rate, and displacement results from all sensitivity models listed in Table 2. As it can be observed, a significant range of results was obtained in terms of their magnitude, variation pattern and time-dependency for pore-pressure, flow rate and displacements. This large variability range of results obtained reflect the sensitivity parametrization done, and thus, uniqueness of the final/best parameter combination cannot be guaranteed. Each sensitivity case is separately presented in the next sections.

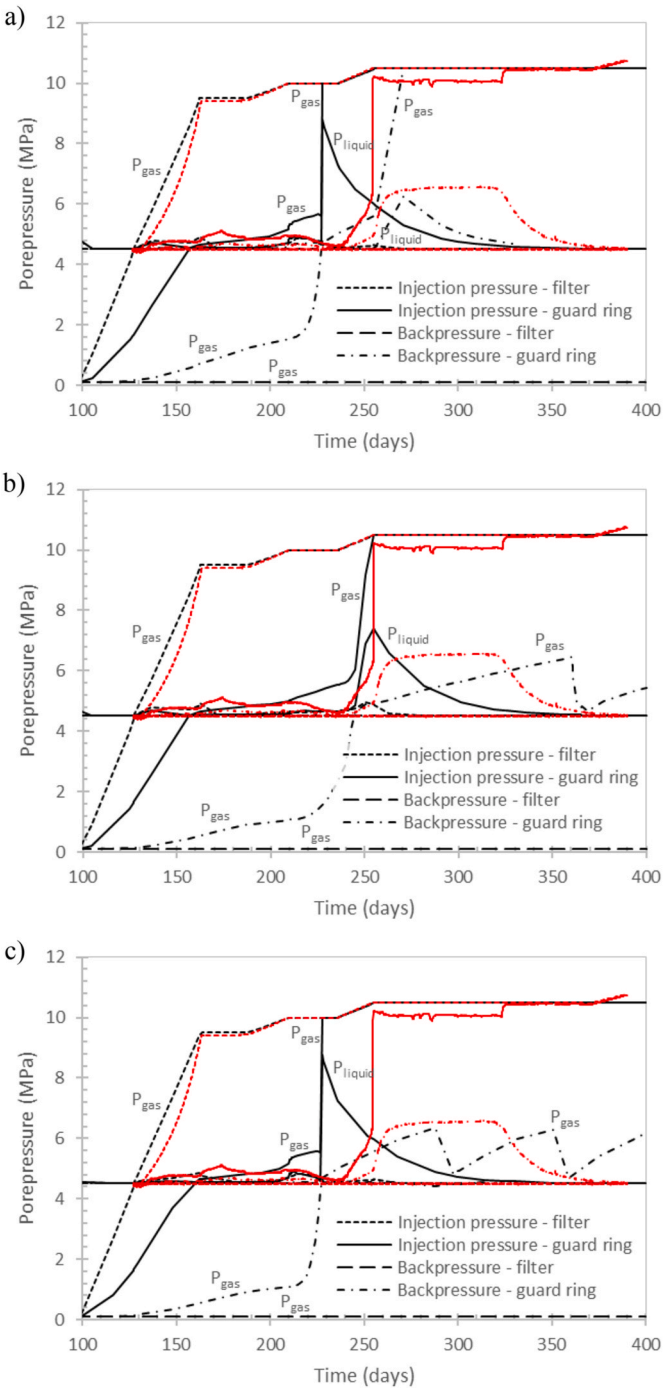

Fig. 21. Evolution of injection pressure and back-pressure for (a) Model D_1 ($E/3$), (b) D_2 (side-flow) and (c) Model D_3 ($E/3$ & side-flow).

4. Results

4.1. Model A (base case)

Fig. 7 shows the evolution of gas pressure at the injection zone and at the guard zone for Model A. As mentioned above, the prescribed injection pressure changes with time. The pressure in the outflow zone is specified at a value of 4.5 MPa. This can be seen in Fig. 7, wherein the results do not display any variation in the outflow or back-pressure. Pressure measurements in the guards indicate a delayed response. It is not until day 290 that the guard on the injection side receives a pressure equal to the injection pressure. An important reduction of the coefficient

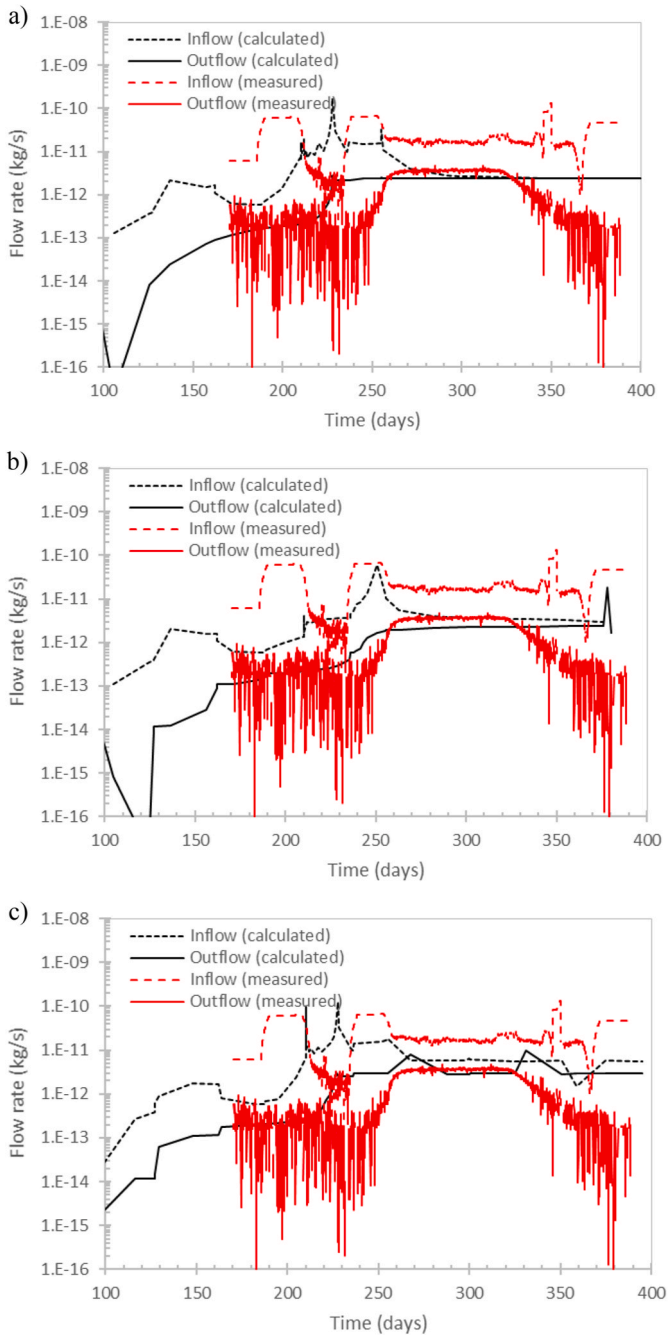

Fig. 22. Gas inflow and outflow rates for (a) Model D_1 ($E/3$), (b) D_2 (side-flow) and (c) Model D_3 ($E/3$ & side-flow).

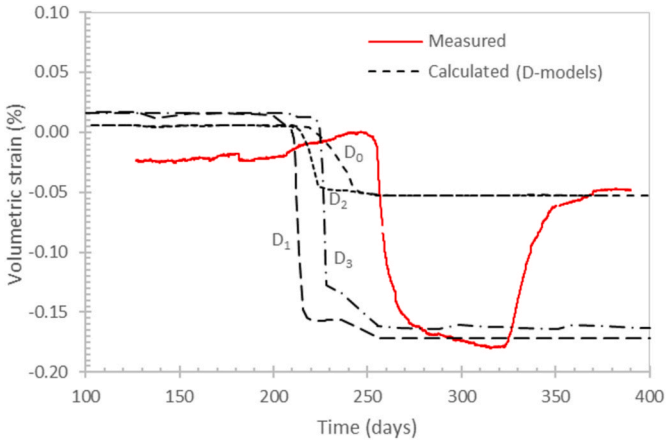

Fig. 23. Comparison of sample volumetric deformation between all D-model cases.

of tortuosity (0.05) has been used to control the dissolved gas diffusion in this case. This means a significant reduction of dissolved-gas effective diffusivity. The use of this coefficient delays the start of the development of gas pressure into the guard. This is consistent with the response observed in the experiment measurements.

Fig. 8 shows the gas inflow and outflow. Inflow into the system displays a maximum once the outflow is fully developed (around 270 days). The peak in inflow also corresponds with the pressurization of the guard near the inflow side. In the long term, inflow and outflow should tend to have a similar (same) value if sample deformation remains constant/stable (and there are no leaks from the experiment) which can be interpreted as a tendency towards steady flow. However, at 400 days (roughly after 250 days of gas injection), steady state has not been reached completely.

Fig. 9 shows displacements and volumetric deformation. The interval around 250 days (for instance, 240–260 days) corresponds to the maximum development of deformations. In this period, the sample is pressurized. Volumetric deformation and radial displacement exhibit the same pattern, while axial movements are very small. Displacements in the radial direction correspond to points at different distances from injection side.

Fig. 10 displays the displacement vectors and deformed mesh evolution as gas flux propagation (by diffusion and advection) progresses through the sample. Fig. 11a and b displays the advective and diffusive distributions of significant gas fluxes. Examining the pore-pressure development (Fig. 8), it can be seen that breakthrough occurs in the 250–300 day range. The two pictures for each flow correspond to times before and after the model gas-flow breakthrough. It is interesting to see that when advection develops, diffusion decreases. Analogously, Fig. 12a and b shows the permeability and degree-of-saturation fields, respectively, which display the response in terms of the generated fluxes before and after the breakthrough. The development of advective fluxes required desaturation and are associated with an increase in intrinsic permeability by deformation due to the opening of the embedded discontinuities that open as the medium expands. At the same time, capillary pressure for desaturation (gas entry value) decrease and facilitated advective gas flow. The resulting desaturation was quite small, which is the expected response for clay-type materials.

4.2. *Model sensitivity to guard-ring volume*

A comparison of models A, B and C is presented in this section. The only difference between the three models is the volume considered for the guard-rings: about 5 ml for case A, 0.2 ml for case B, and no guard-ring volume for case C. This is an annular volume on the inflow and outflow surfaces, connected to different pressure sensors. Gas took some time to develop pressure in the guard-rings. It is expected that the larger the guard-ring volume is, the longer the delay of gas-pressure

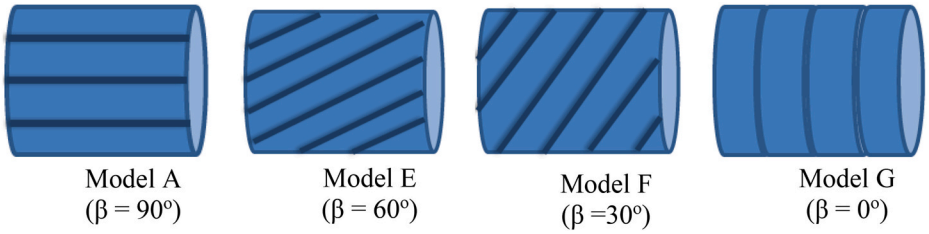

Fig. 24. Anisotropy cases assumed: bedding layered varies from axial/parallel (Model A; original model assumption with β-angle of 90°), tilted (Models E and F), and radial/orthogonal (Model G) orientations with regards to sample's axial direction.

development at the guard-ring zone close to injection. This delay depends on gas migration properties (i.e., tortuosity) as well as on the guard-ring volume considered (as it is known that the resulting data reception may be influenced by the existent volume between the sample -i.e., actual occurrence of the response development- and the sensor –i.e., the received/appearance of the response development-). The gas tortuosity considered in the A, B and C models was maintained at 0.05. The effect on the time to reach the pressure in the guard-ring gave different results for different assumed guard-ring volumes. As it can be observed in Model C, the absence of guard-ring volume produced an earlier development of the pressure in the guard-ring zone, for the same tortuosity, compared to Models A and B.

Fig. 13 shows the gas pressure evolution comparison between the different guard-ring volume assumptions (i.e., models A, B and C). As it can be observed, the increase of guard-ring volume factor is proportional to the time required to achieve the gas-pressure response at the guard-rings. According to the results obtained from the test, the guard-ring volume factor that best matches the experimental data (i.e., detection of injection pressure at guard-ring locations at about 250 days) is around VF = 0.2, which corresponds to an actual volume of 2 ml.

From the experimental results, it can be seen that the back-pressure filter is draining at a pressure much lower than the injection gas pressure. Therefore, the model does not capture well the pressure development in the guard-ring at the back-pressure side. The model with no guard-ring (or guard-ring volume equal to zero; Model C) does not accumulate as much gas as in the other cases, as the sample had less pore space between the injector and the lateral boundaries, and between the injection and back-pressure locations in comparison with Models A and B.

Fig. 14 shows the inflow and outflow response. The presence of the guard-ring volume allows some gas to accumulate, which can be understood as the difference between the accumulated inflow and outflow gas curves (see Fig. 15). This relates to accumulated gas in the sample due to the sample volumetric dilation. This effect was clearly observed in the experiment results as well as in the models with guard-ring volumes.

Displacements in the radial direction at different distances from injection are in the range of 20 μm and develop in step with pressure development (Fig. 16). Effective stress decreases (total stress is constant, but fluid pressure increases) producing an expansion or dilation of the sample. Fig. 17 shows that a net volumetric expansion is calculated. The axial displacement changes before gas injection but does not respond in the same way as the radial displacement. Comparison with measurements indicate that the response corresponds well with the experimental data in time, but it underestimates its magnitude.

4.3. Model sensitivity to diffusivity

Model B and Model D were used to analyze the effect of the dissolved gas diffusion effect only. For a coefficient of tortuosity equal to 1, diffusivity is at a maximum. Model B with tortuosity coefficient of 0.05 is compared with Model D with a tortuosity coefficient of 0.10. Model B and Model D_0 have the same guard-ring volume factor of 0.2. As it can be observed in Fig. 18, for Model D (with a higher tortuosity coefficient), the pressure development in the guard-rings takes place earlier than in Model B. The lower the coefficient of tortuosity was, the larger the delay of gas-pressure development was obtained in the guard-ring close to injection zone. However, the guard-ring back-pressure response increases to the same maximum level as the injection pressure. This behavior was not observed in the test, where the back-pressure increased at the same moment as the injection (breakthrough point) but to a lower pore-pressure value, then remained almost constant for 50–60 days, and then returned back to the initial pore-pressure condition value (i.e., confinement pressure). The first assumed tortuosity value is low (i.e., $\tau = 0.05$). Actually, if the guard-ring elements (and related inherent volume) are not explicitly modelled −as in Model C− a much lower tortuosity value would be required (i.e., $\tau < 0.05$) to get a realistic delay in the development of pressure at the guard-ring zone.

Fig. 19a displays the calculated fluxes. The increase of the coefficient of tortuosity implies, for an equivalent time, a larger outflow. For instance, at 200 days, outflow is about twice in the case of a twofold increase of the coefficient of tortuosity. As breakthrough occurs, advection becomes dominant, and the flux difference between inflow and outflow becomes smaller because diffusion become less relevant. Fig. 19b shows that the gas accumulation in the case of a higher coefficient of tortuosity is lower. The higher mobility of the gas implies less accumulation in the guard-rings.

Displacements in the radial direction at different distances from injection are in the range of 20 μm and develop according to pressure development (Fig. 20a). Effective stress decreases (total stress is constant but fluid pressure increases) which produces expansion or dilation of the sample. Fig. 20b shows the computed volumetric deformation. Axial displacement changes before gas injection but does not respond in the same way as radial displacements.

Model D_0 was considered as the best fitting case for pore-pressure results because pressure generation/response at both injection filter and injection guard-ring was obtained at almost the same time frame as measurements did (see Fig. 18). However, the obtained response of pore-pressure reduction at the backpressure filter was not captured (neither it was in any other previous model). Furthermore, sample deformations were not properly captured either, which may indicate that material stiffness should be reduced from the initial material assumptions (Table 1). As specified in Table 2, Model D_1 presents results with a reduced stiffness ($E_{D1} = E_{D0}/3 = 2833$ MPa; more consistent stiffness values with those from ,[6] and the ones assumed also by Yang et al.[11] and Model D_2 includes higher permeability at the backpressure side (i.e., $k_{ii} = 1 \times 10^{-18}$ m^2 at the sample's border surface in contact with the backpressure guard-ring and filter to allow a flow connectivity sensitivity case between both elements). Model D_3 includes both variations from D_1 and D_2 (i.e., less stiffness and side-flow case). Figs. 21–23 presents the pore-pressure, flow rates, and volumetric strain results obtained for these $D_{1\text{-}3}$ model variations. Not surprisingly, both cases with stiffness reduction (i.e., models D_1 and D_3) generated a significant increase of the volumetric strains, better fitting the maximum values obtained in the measurements (see Fig. 23). But, on the other hand, an earlier gas and liquid pressures were obtained at the injection guard-ring

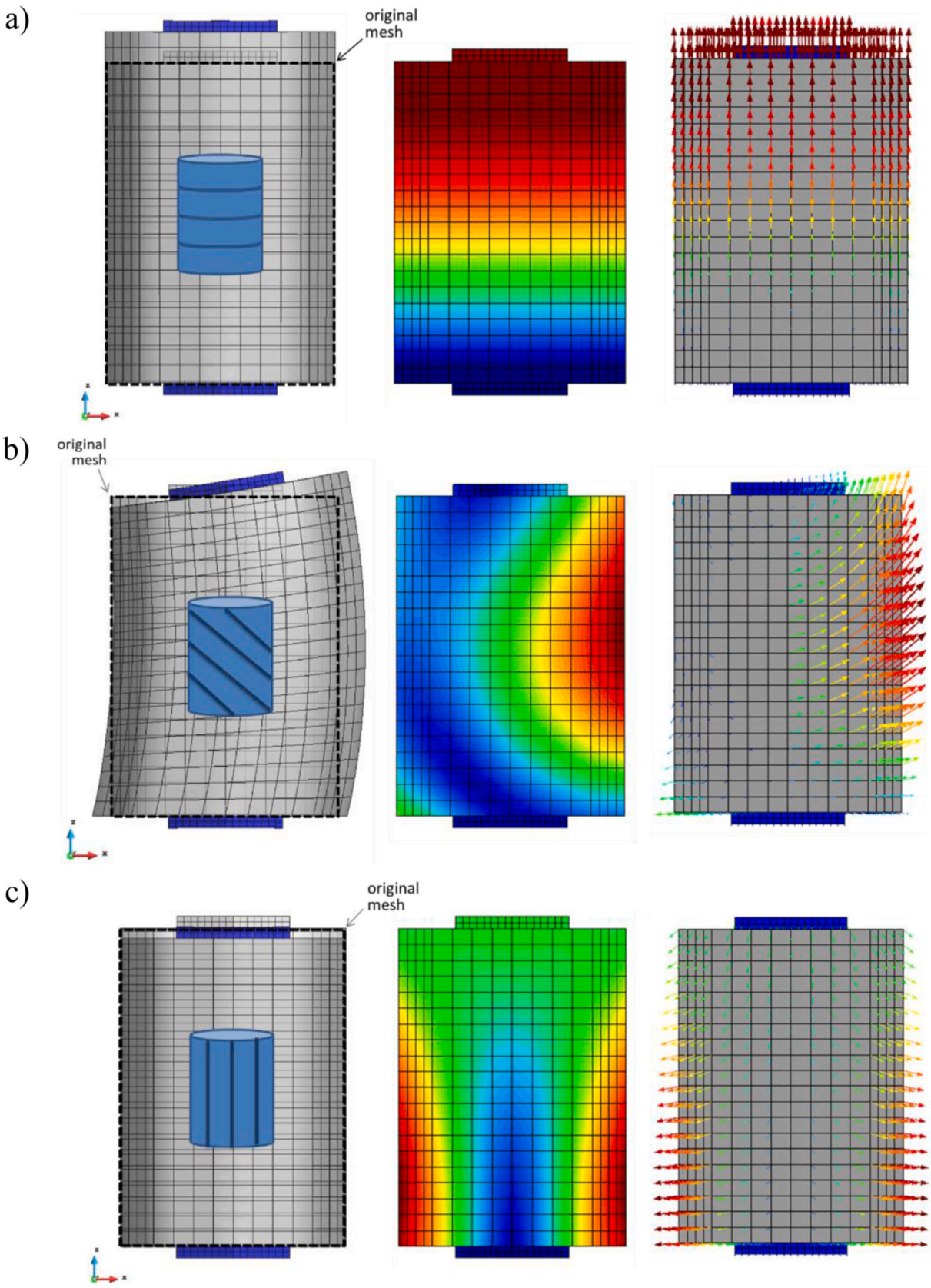

Fig. 25. Qualitative effect of layered bedding orientation: (a) $\beta = 0^{\circ}$, (b) $\beta = 45^{\circ}$, and (c) $\beta = 90.^{\circ}$

a) Model E (β = 60°)

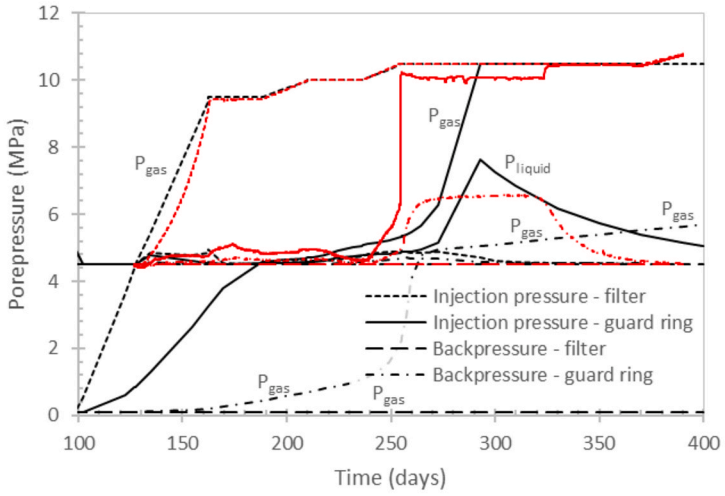

b) Model F (β = 30°)

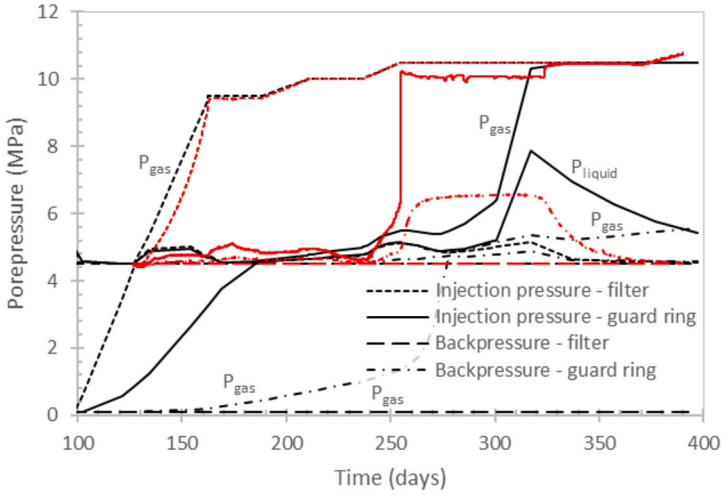

c) Model G (β = 0°; bedding perpendicular to sample's axial direction)

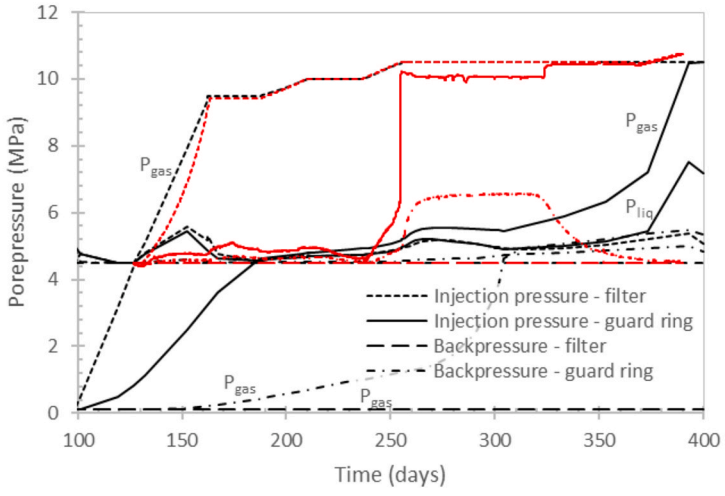

Fig. 26. Comparison of pressures for Models E, F and G.

a) Model E (β = 60°)

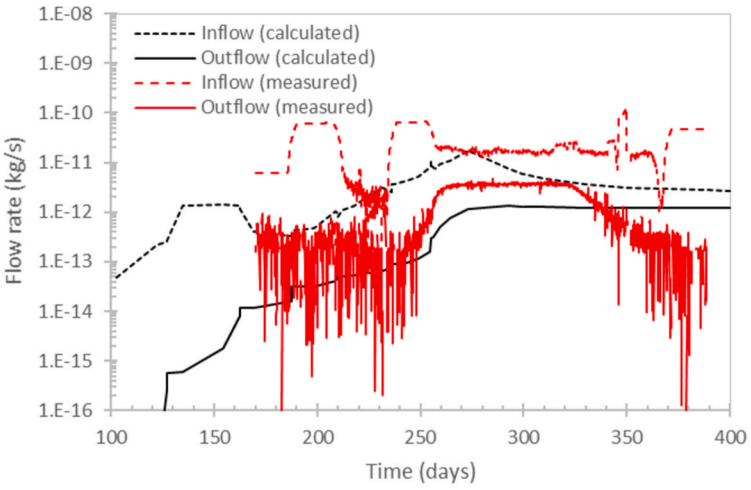

b) Model F (β = 30°)

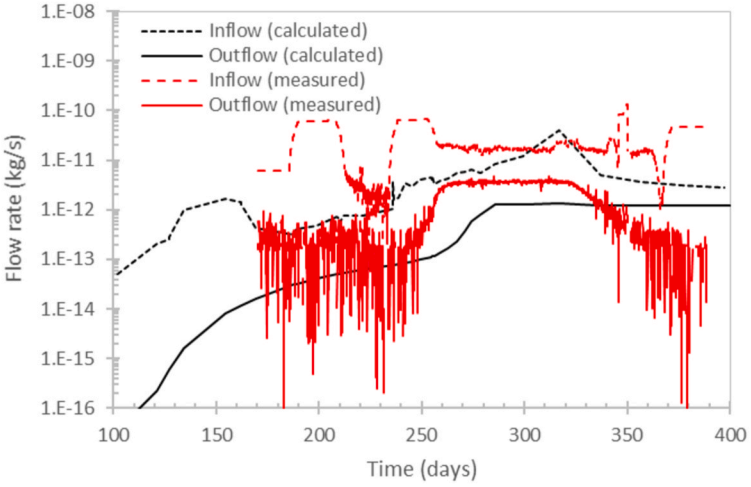

c) Model G (β = 0°; bedding perpendicular to sample's axial direction)

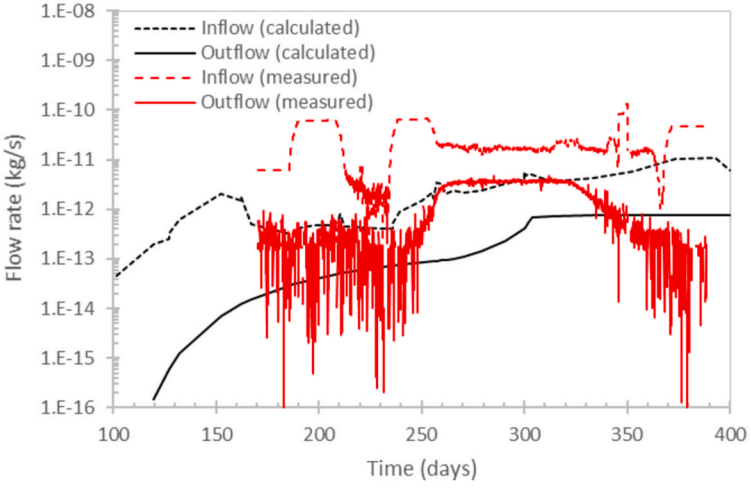

Fig. 27. Comparison of gas inflow and outflow rates for Models E, F and G.

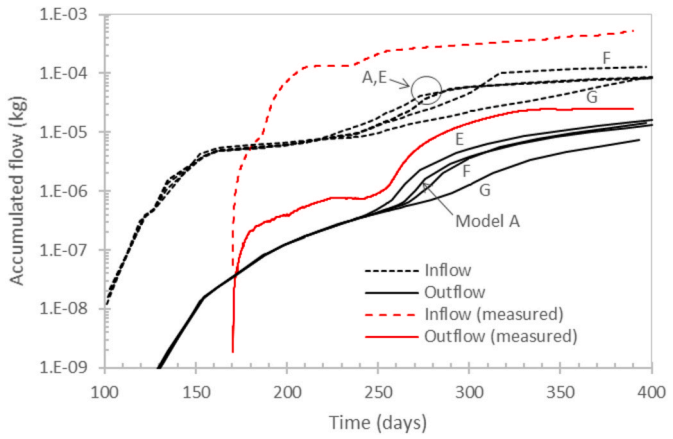

Fig. 28. Comparison of accumulated gas inflow and outflow for Models A, E, F and G (experimental values have been integrated from 165 days). Sensitivity on material anisotropy according to the sample bedding planes direction.

(see Fig. 21a and c). As shown in Fig. 22, the obtained flow rates were similar as the ones obtained in previous models, even for the side-flow allowance cases (i.e., models D_2 and D_3). However, what is interesting to see it that the side-flow allowance (or easier flow connectivity between the backpressure guard-ring and filter) generated a reduction of the gas pressure (see Fig. 21). This can be hypothesized to be similar to what happened in the measurements at about day 325. This gas pressure reduction obtained by the model has not the same 60 days flat-plateau-shape duration as in the measurements, but indicates that the effect may be achieved by the same/similar side-flow once the sample contains enough gas pressure at the back-end. It should be noticed that both D_2 and D_3 models (i.e., represented in Fig. 21b and c, respectively), properly capture the maximum gas pressure obtained at backpressure guard-ring (i.e., up to about 6.5 MPa), but with less sharp vertical pressure generation, and with an oscillating trend (see Fig. 21c). This reduction effect was also captured in displacement and volumetric strain measurements, whereas in Models D_2 and D_3 it was captured in the pore-pressure results only.

4.4. Model sensitivity to the direction of anisotropy

The original COx sample tested had bedding direction defined by BGS (parallel to sample's axial direction). In spite of this, sensitivity to anisotropy has been carried out to analyze its influence on the results.

Models E, F and G were developed by changing the orientation of the anisotropy axis, which implies changes in permeability and deformability of the sample. The anisotropy (bedding layered orientation) was changed to 90°, 60° and 30° (see Fig. 24). For the three models analyzed here, guard-ring volume factor and tortuosity were equal to those in Model A (i.e. VF = 0.5 and $\tau = 0.05$). As an example, Fig. 25 displays the qualitative deformed mesh and displacements assuming 0°, 45° and 90° layered bedding orientation (β).

Fig. 26 displays the effect of changing the direction of lower permeability and higher deformability from radial to axial on pore-pressure development. For cases A and E, the connection between inflow and outflow sides is higher due to the larger permeability in the axial direction. Although there are appreciable differences on pore-pressure development, Fig. 27 shows that fluxes are not significantly different between the bedding orientation cases analyzed. If calculated fluxes are similar, the accumulated volume of gas in the system is also similar (see Fig. 28).

Displacements in the radial direction (Fig. 29) at different distances from injection are in the range of 20–50 μm and develop according to pressure development. Effective stress decreases (total stress is constant, but fluid pressure increases) which produces expansion or dilation of the sample. Depending on the anisotropy orientation, radial displacements are negligible (bedding perpendicular to axial direction; Model G) or maximum (for inclined bedding; models E and F). Axial displacement is maximized for bedding perpendicular to the axial direction.

5. Conclusions

In this study, a 3D hydro-gas-mechanical (HGM) finite element (FE) model has been developed and the available measurements from a triaxial fluid injection test on Callovo-Oxfordian (COx) claystone have been compared with the numerical results obtained in the analyses.

Several models have been developed in order to understand the importance of several factors with respect to gas migration. This paper contains a selected set of models that illustrate its sensitivity on tortuosity of dissolved gas, guard-ring volume and sample orientation. All the presented models share a common configuration in terms of initial heterogeneity, boundary and initial conditions, fluid injection protocol, and meshing.

A significant variation of the arrival time for gas pressure in guard-rings is observed in the different models. The incorporation of the guard-rings volume into the model (which generates more available pore space in which gas can accumulate) has been crucial to represent the delay of gas pressure build-up. Different guard-ring volume assumptions, modelled through a volume factor (VF), generate different breakthrough times: the smaller the VF is, the earlier the pore-pressure is generated at the injection guard-ring with regards to pressure reaction at the injection filter. Also a reduced tortuosity coefficient with respect to the default value is required to obtain a realistic breakthrough delay.

As the comparison with measured displacement and volumetric deformation show, deformability is somewhat underestimated in some cases though the trends, time development and the difference between initial and final strains are well captured. A lower material stiffness is required to capture the magnitude of the maximum measured volumetric strain.

Experimental results show a gas pressure development and a decay −with an intermediate/sustained flat plateau of about 60 days− at the guard-ring close to back-pressure and deformation recovery. These effects are difficult to explain with the current model. In fact, it is not clear what occurred in the experiment since injection pressure remains high, outflow decreases, pressure in the back-pressure side decreases and, consequently, volumetric deformation recovers. However, a similar decay effect can be obtained by assuming a higher permeability at the backpressure side of the sample (surface in contact with the back-pressure guard-ring and filter), allowing gas flow connectivity between both guard-rings and filter components by side-flow, once the sample reaches a certain inner pressure. Nonetheless, this effect is only captured by the model in the pore-pressure results, but not in the volumetric deformation nor in the displacements (lateral/axial) of the sample.

The complex problem of gas propagation through clay based materials is investigated in extreme conditions of gas flow rates and pressurization. From the experiments and the models under these conditions, it is difficult to draw conditions for the performance assessment. What these tests and models permit is to demonstrate whether the processes are understood or not. A future calculation of scenarios of waste disposal must be done with models that include these processes but the activation may depend on the pressurization conditions.

Declaration of competing interest

The authors declare that they have no known competing financial interests or personal relationships that could have appeared to influence the work reported in this paper.

a) Model E (β = 60º)

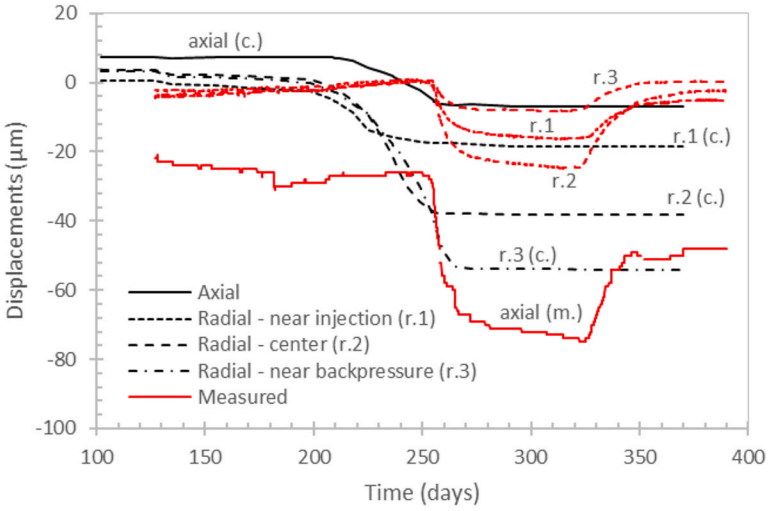

b) Model F (β = 30º)

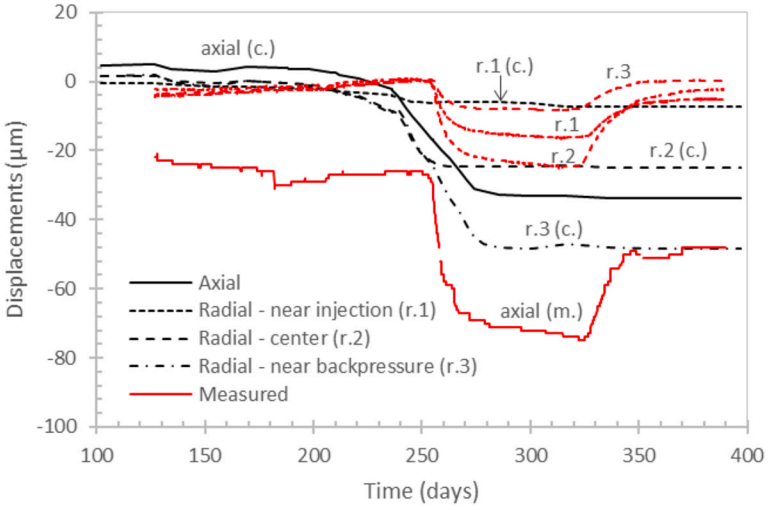

c) Model G (β = 0º; bedding orthogonal to sample's axial direction)

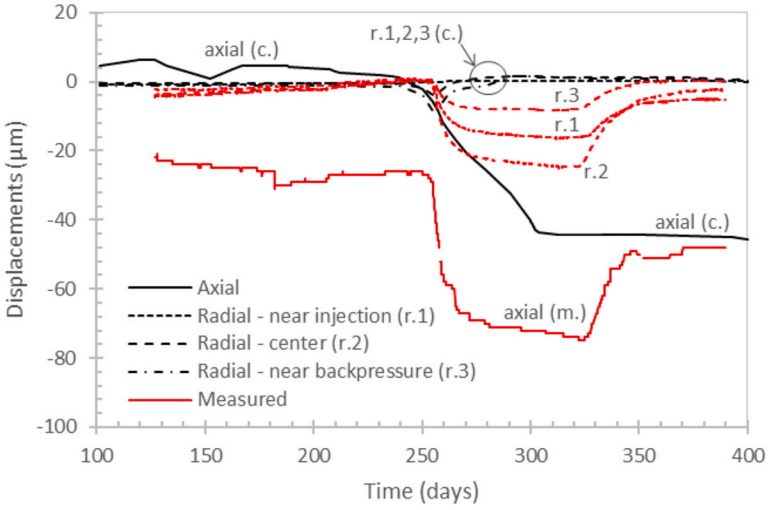

Fig. 29. Comparison of radial and axial displacements for Models E, F and G.

Data availability

Data will be made available on request.

Acknowledgments

DECOVALEX is an international research project comprising participants from industry, government and academia, focusing on development of understanding, models and codes in complex coupled problems in sub-surface geological and engineering applications; DECOVALEX-2019 is the current phase of the project. The authors appreciate and thank Andra for funding this work, as well as all DECOVALEX-2019 Funding Organizations Andra, BGR/UFZ, CNSC, US DOE, ENSI, JAEA, IRSN, KAERI, NWMO, RWM, SÚRAO, SSM and Taipower for their financial and technical support of the work described in this report.

The authors wish to acknowledge Elena Tamayo-Mas, Jon Harrington, Jean Talandier, Gilles Armand and Alex Bond for their constructive comments and discussions during the modelling work carried out in the context of DECOVALEX-2019, as well as the reviewers of the manuscript during the submission process of this study, which allowed to substantially improve the paper in a clear way.

The authors wish also to acknowledge the support of the International Centre for Numerical Methods in Engineering (CIMNE) and the funding received from the Spanish Ministry of Economy and Competitiveness through the "Severo Ochoa Programme for Centres of Excellence in R&D" (CEX2018-000797-S).

The statements made in the report are, however, solely those of the authors and do not necessarily reflect those of the Funding Organizations.

References

1 Marschall P, Gimmi T, Horseman S. Characterisation of Gas Transport Properties of the Opalinus Clay, a potential host rock formation for radioactive waste disposal. *Oil Gas Sci Technol*. 2005;60:121–139. https://doi.org/10.2516/ogst:2005008.

2 Harrington J, De la Vaissière R, Noy D, Cuss R, Talandier J. Gas flow in Callovo-Oxfordian claystone (COx): results from laboratory and field-scale measurements. *Mineral Mag*. 2012;76(8):3303–3318. https://doi.org/10.1180/minmag.2012.076.8.43.

3 Arnedo D, Alonso E, Olivella S. Gas flow in anisotropic claystone: modelling triaxial experiments. *Int J Numer Anal Methods GeoMech*. 2013;37(14), 0363-9061: 2239–2256.

4 Menaceur H, Delage P, Tang AM, Conil N. The thermo-mechanical behaviour of the Callovo-Oxfordian claystone. *Int J Rock Mech Min Sci*. 2015;78:290–303. https://doi.org/10.1016/j.ijrmms.2015.07.002.

5 Armand G, Conil N, Talandier J, Seyedi DM. Fundamental aspects of the hydromechanical behaviour of Callovo-Oxfordian claystone: from experimental studies to model calibration and validation. *Comput Geotech*. 2017;85:277–286. https://doi.org/10.1016/j.compgeo.2016.06.003.

6 Desbois G, Höhne N, Urai JL, Bésuelle P, Viggiani G. Deformation in cemented mudrock (Callovo-Oxfordian clay) by microcracking, granular flow and phyllosilicate plasticity: insights from triaxial deformation, broad ion beam polishing and scanning electron microscopy. *Solid Earth*. 2017;8(2):291–305. https://doi.org/10.5194/se-8-291-2017.

7 Zhang C, Rothfuchs T. Experimental study of the hydro-mechanical behaviour of the Callovo-Oxfordian argillite. *Appl Clay Sci*. 2004;26(1-4):325–336. https://doi.org/10.1016/j.clay.2003.12.025.

8 Belmokhtar M, Delage P, Ghabezloo S, Tang A-M, Menaceur H, Conil N. Poroelasticity of the callovo-oxfordian claystone. *Rock Mech Rock Eng*. 2017;50: 871–889. https://doi.org/10.1007/s00603-016-1137-3.

9 Zhang C, Armand G, Conil N, Laurich B. Investigation on anisotropy of mechanical properties of Callovo-Oxfordian claystone. *Eng Geol*. 2019;251:128–145. https://doi.org/10.1016/j.enggeo.2019.02.008.

10 Shi HL, Hosdez J, Rougelot T, Xie SY, Shao JF, Talandier J. Influences of structural anisotropy and heterogeneity on three-dimensional strain fields and cracking patterns of a clay-rich rock (2021). *Acta Geotechnica*. 2021;16:2175–2187. https://doi.org/10.1007/s11440-021-01152-6.

11 Mahjoub M, Rouabhi A, Tijani M, Talandier J. Numerical study of Callovo-Oxfordian argillite expansion due to gas injection. *Int J GeoMech*. 2018;18, 04017134. https://doi.org/10.1061/(ASCE)GM.1943-5622.0001050.

12 Yang J, Fall M, Guo G. A three-dimensional hydro-mechanical model for simulation of dilatancy controlled gas flow in anisotropic claystone. *Rock Mech Rock Eng*. 2020; 53:4091–4116. https://doi.org/10.1007/s00603-020-02152-w.

13 Cuss R, Harrington J. *Update on Dilatancy Associated with Onset of Gas Flow in Callovo-Oxfordian Claystone; Progress Report on Test SPP_COx-2*. British Geological Survey, Minerals and Waste Programme; 2011. Commissioned Report Cr/11/110.

14 Cuss R, Harrington J, Giot R, Auvray C. Experimental observations of mechanical dilation at the onset of gas flow in Callovo-Oxfordian claystone. *Geological Society London Special Publications*. 2014;400(1):507. https://doi.org/10.1144/SP400.26.

15 Harrington JF, Graham SC, Cuss RJ, Norris S. Gas network development in a pre-compacted bentonite experiment: evidence of generation and evolution. *Appl Clay Sci*. 2017;147:80–89. https://doi.org/10.1016/j.clay.2017.07.005.

16 Damians IP, Olivella S, Gens A. Modelling gas flow in clay materials incorporating material heterogeneity and embedded fractures. *I Int J Rock Mech Min Sci*. 2020;136, 104524. https://doi.org/10.1016/j.ijrmms.2020.104524.

17 Ramajo H, Olivella S, Carrera J, Sanchez-Vila X. Simulation of gas dipole tests in fractures at the intermediate scale using a new upscaling method. *Transport Porous Media*. 2002;46:269–284.

18 Tamayo-Mas E, Harrington JF, Brüning T, et al. Modelling advective gas flow in compact bentonite: Lessons learnt from different numerical approaches. *Int J Rock Mech Mining Sci*. 2021;139. https://doi.org/10.1016/j.ijrmms.2020.104580. In this issue.

19 Olivella S, Alonso EE. Gas flow through clay barriers. *Geotechnique*. 2008;58: 157–168. https://doi.org/10.1680/geot.2008.58.3.157.

20 Harrington J, Cuss R, C Graham S. *British Geological Survey (BGS), Radioactive Waste Management Limited*. ENGINEER (modElliNg Gas INjection ExpERiments); 2016. DECOVALEX 2019, Specs. for Task A.

21 Olivella S, Gens A, Carrera J, Alonso E. Numerical formulation for a simulator (CODE-BRIGHT) for the coupled analysis of saline media. *Eng Comput*. 1996;13(7): 87–112. https://doi.org/10.1108/02644409610151575.

22 CODE_BRIGHT. *CODE_BRIGHT User's Guide. Department of Civil and Environmental Engineering (DECA), Barcelona School of Civil Engineering, Department of Civil and Environmental Engineering (DECA)*. Universitat Politècnica de Catalunya·BarcelonaTech (UPC), and International Centre for Numerical Methods in Engineering (CIMNE); 2021. https://deca.upc.edu/ca/el-departament/seccions/etcg/recerca/projectes/code_bright. https://www.gidhome.com/gid-plus/modules/modules-research/27/codebright/.

23 Carman PC. *Fluid Flow through Granular Beds. Transactions*vol. 15. London: Institution of Chemical Engineers; 1937:150–166.

24 Olsson R, Barton N. An improved model for hydromechanical coupling during shearing of rock joints. *Int J Rock Mech Min Sci*. 2001;38(No. 3):317–329.

25 Olivella S, Gens A. Double structure THM analyses of a heating test in a fractured tuff incorporating intrinsic permeability variations. *Int J Rock Mech Min Sci*. 2005;42: 667–679.